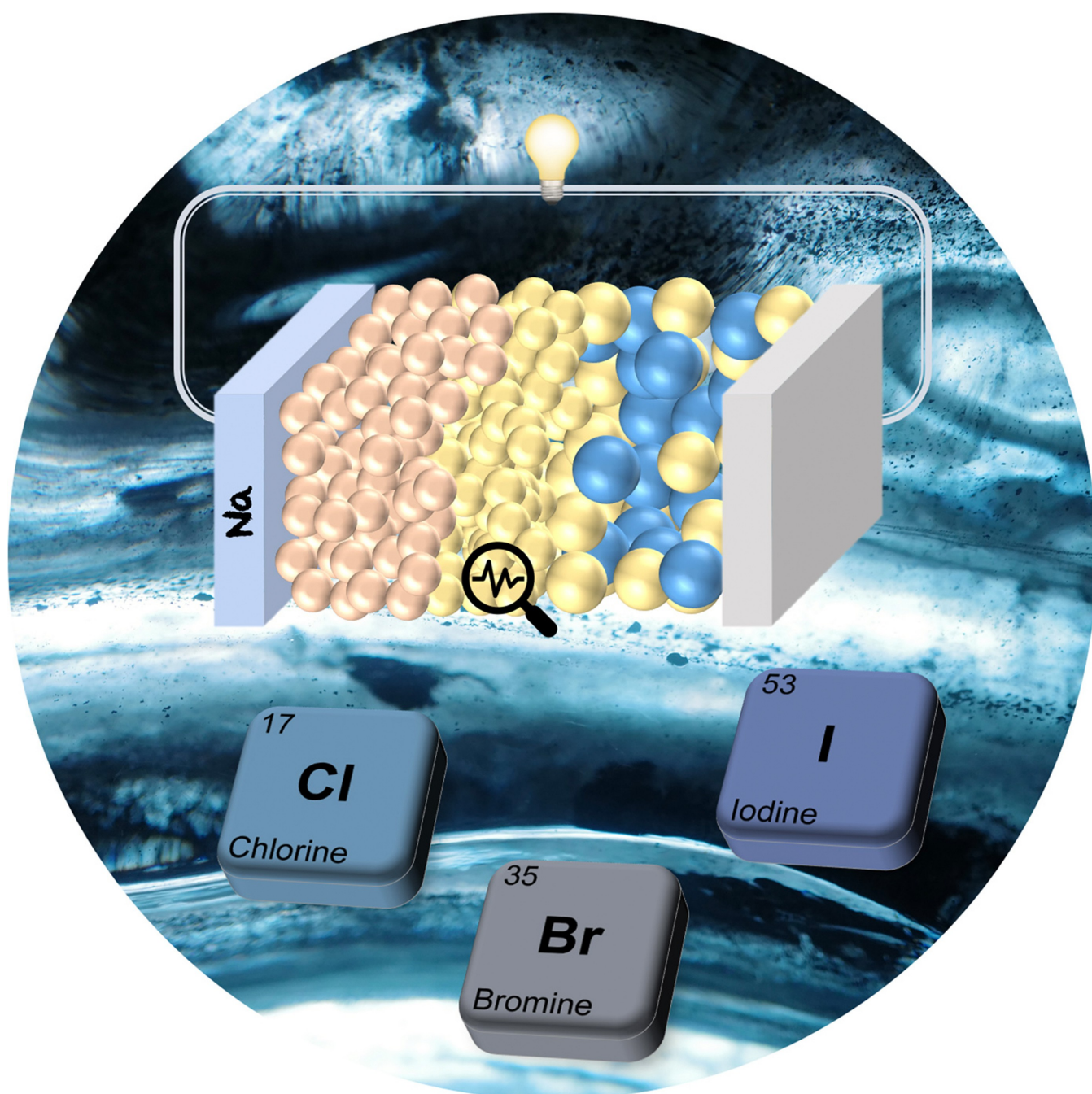


Emerging Halide Solid Electrolytes for Sodium Solid-State Batteries: Structure, Conductivity, Paradigm of Applications

Zhixuan Wei,*^[a] Linda F. Nazar,*^[b] and Jürgen Janek*^[a]



Solid-state sodium batteries (SSSBs) hold great promise for the development of safe, low-cost energy storage devices. Developing solid electrolyte (SE) materials with high ionic conductivity, high chemical and electrochemical stability, as well as good mechanical properties is the most critical step. As a promising category of SEs, halide-based solid electrolytes combine good ionic conductivity and good electrochemical stability, and they have been already widely studied for their use in lithium-based

solid-state batteries. In contrast, knowledge of their sodium analogues is still limited. Here, we provide a comprehensive overview of halide SEs for sodium ion conduction with a perspective of both experimental and theoretical studies, including the correlation of structure and properties; sodium ion conductivity and diffusivity; as well as compatibility with electrode materials. We hope this perspective can stimulate more research in developing halide-based SSSBs.

1. Introduction

Sodium-ion batteries (SIBs) are considered as one of most promising additions to lithium-ion battery (LIB) technology owing to the earth-abundance and cost-effective nature of sodium, particularly in the light of the growing emphasis on sustainability.^[1–3] Given the close relationship between sodium and lithium in terms of physical/chemical properties, the development of SIBs has been accelerated by leveraging advancements in LIB technologies. Encouragingly, several projects on the commercialization of SIBs have already been undertaken with the purpose of complementing LIBs, especially for stationary energy storage.^[4] Nevertheless, the use of flammable and volatile organic liquid electrolyte has raised safety concerns. To address this, replacing the liquid electrolyte with inorganic solid-state electrolytes as the separator may suppress thermal runaway, and thus enhance the safety properties of the battery.^[5] In addition, the solid-state sodium-ion battery (SSSBs) configuration can enable high-voltage cathodes, the sodium metal anode, as well as easy-to-direct stacking architectures to achieve higher energy density.^[6–9] To achieve satisfactory electrochemical properties of SSSBs, the prerequisite is to develop solid-state sodium-ion conductors with the following characteristics: high ionic conductivity, high electronic resistance, good chemical and electrochemical stability, good mechanical properties, interface compatibility with other cell components, etc.^[10,11] Several groups of inorganic solid electrolyte (SE) materials have been developed, mostly based on oxides and sulfides. Oxide SEs (β -alumina,^[12,13] NaSICONs,^[14–16] etc.) generally exhibit superior chemical stability and a wide electrochemical stability window, but the ionic conductivity is limited to 10^{-3} Scm⁻¹, and demanding sintering conditions are required, which could also induce large grain boundary

resistance. On the contrary, sulfide SEs ($\text{Na}_{11}\text{Sn}_2\text{PS}_{12}$,^[17,18] Na_3PS_4 ,^[19,20] Na_3SbS_4 ,^[21,22] etc.) demonstrate superionic conductivity, and electrode composites can be prepared by simple cold-pressing methods. The room temperature (hereafter denoted as RT) ionic conductivity of tungsten-substituted Na_3SbS_4 can even reach 41 mScm⁻¹, which is among the highest reported for any alkali ion electrolyte.^[23] Nevertheless, the intrinsic narrow electrochemical stability window limits the choice of cathode materials, and causes pronounced side reactions at the cathode/electrolyte interface. In addition, the SE is also unstable against the sodium metal anode.^[24,25]

In the past five years, lithium metal halide SEs (Li_3MCl_6 , where M=Y, In, Er, Sc, etc.) have attracted growing research interest owing to a combination of high ionic conductivity and a wide electrochemical stability window.^[26,27] Compared with oxides and sulfides, the monovalent nature of chloride ions weakens the Coulomb interaction between Li^+ ions and the anion sublattice, smoothing the energy landscape and facilitating ion migration.^[28] In principle, Li_3MCl_6 phases exhibit two types of anion sublattice structures with either hexagonal close packing (*hcp*) or cubic close packing (*ccp*). The crystal structure types can be further divided into trigonal, orthorhombic and monoclinic systems, with the structure being somewhat dependent on the ionic radius of M³⁺.^[29] In 2018, Asano et al. reported Li_3YCl_6 and Li_3YBr_3 as SEs, which exhibit *hcp*-trigonal and *ccp*-monoclinic structures, respectively.^[30] A high RT ionic conductivity of $\sigma(\text{Li}^+)=1.7$ mScm⁻¹ for highly crystalline Li_3YBr_3 was attained; and superior oxidation stability up to 4.5 V (vs. Li⁺/Li) for Li_3YCl_6 with $\sigma(\text{Li}^+)=0.51$ mScm⁻¹ was reported, which was considered groundbreaking. Subsequently, strategies such as aliovalent atom substitution,^[31–33] tuning cation disorder^[34] and introducing stacking faults^[35] have been used to further (modestly) increase the RT ionic conductivity of lithium halide SEs. In addition, the ion migration behavior in halide lattices has also been investigated in detail.

The development of Na halide SEs, on the other hand, is further behind. To date, $\text{Na}_{3-x}\text{Er}_{1-x}\text{Zr}_x\text{Cl}_6$,^[36] $\text{Na}_{3-x}\text{Y}_{1-x}\text{Zr}_x\text{Cl}_6$,^[37,38] $\text{Na}_{2+x}\text{Zr}_{1-x}\text{In}_x\text{Cl}_6$,^[39] Na_2ZrCl_6 ,^[40] and NaAlCl_4 ,^[41] have been synthesized, yet the highest reported ionic conductivities only reach $\sigma(\text{Na}^+) \approx 10^{-5}$ Scm⁻¹. Very recently, the amorphization of Na-TaCl₆ led to Na⁺-ion conductivity on the order of mScm⁻¹.^[42] The proof-of-concept SSSBs reported above using Na halides as a catholyte exhibit highly reversible behavior, with good capacity retention during long cycling tests, which encourages us to review the state-of-the-art in this field, to better understand the current challenges and bottlenecks.

[a] Dr. Z. Wei, Prof. Dr. J. Janek

Institute of Physical Chemistry & Center for Materials Research, Justus Liebig University Giessen, Heinrich-Buff-Ring 17, 35392 Giessen, Germany
 E-mail: Zhixuan.Wei@phys.chemie.uni-giessen.de
 Juergen.Janek@phys.chemie.uni-giessen.de

[b] Prof. L. F. Nazar

Department of Chemistry and the Waterloo Institute for Nanotechnology, University of Waterloo, 200 University Avenue West, Waterloo, Ontario N2L 3G1 Canada
 E-mail: Ifnazar@uwaterloo.ca

© 2024 The Authors. *Batteries & Supercaps* published by Wiley-VCH GmbH. This is an open access article under the terms of the Creative Commons Attribution Non-Commercial NoDerivs License, which permits use and distribution in any medium, provided the original work is properly cited, the use is non-commercial and no modifications or adaptations are made.

In this review, we provide a comprehensive overview on the existing literature on sodium halide solid electrolytes, covering both experimental work and theoretical studies. The synthesis-structure-property correlations of different chlorides are presented. The crystal structures and predicted ionic transport properties of several bromides and iodides are summarized. First though, we revisit several early investigations on sodium ternary halide compounds with respect to Na^+ ion conduction. We hope that the summarized information can contribute to the further development of sodium halide electrolytes and stimulate exploration of new sodium halide SE materials.

2. Early Study of Ternary Sodium Halide Compounds as Na-Ion Conductors

2.1. $\text{UCl}_6/\text{UCl}_3$ -Type

The earliest attempts to explore Na-based halides as sodium SEs date back to the 1980s. Fouque et al. synthesized Na_2UBr_6 and observed Na^+ ion conduction at 652 K and 663 K.^[43] Bogacz et al. found that its structure is a derivative of the UCl_6 -structure.^[44] In this reference material, UCl_6 crystallizes in a trigonal lattice with space group $P\bar{3}m1$ (Figure 1a), where the chlorine atoms stack to form a hexagonal close packed lattice and uranium atoms partially occupy 1/6 of the octahedral interstices. When sodium cations are introduced – e.g. in forming Na_2UBr_6 – the uranium valence state is reduced from +6 to +4 to keep charge balance, and Na^+ ions occupy some of the vacant sites without altering the basic “ UCl_6 ” halide framework. Due to the presence of remaining unoccupied sites and the possibility of UBr_6 librational motion, Na^+ ion

conduction becomes feasible. Indeed, Rietveld refinement against neutron powder diffraction data revealed that half of the octahedral interstitial sites remain unoccupied, facilitating the diffusion of Na^+ ions. With increasing temperature, Na_2UBr_6 undergoes a phase transition, which affects the ionic conductivity.^[45] At 657 K, the original trigonal cell becomes slightly distorted to form an orthorhombic cell, and the occupation of the cations in the octahedral interstices changes. The libration of the UBr_6 unit, which can be described as wiggling motions of rigid octahedra, opens up the channels between Na^+ sites in one direction, and induces a sharp increase in the ionic conductivity in this intermediate phase. With an increase in temperature to 695 K, a structure with higher symmetry results from the rotation of the UBr_6 octahedra (in different orientation compared to the orthorhombic cell), forming a body-centred cell. In this configuration, the Na^+ ions are no longer localized in the interstices of the halogen sublattice. This, together with the UBr_6 libration further improves the ionic conductivity to values of about $\sigma(\text{Na}^+) \approx 20 \text{ mS cm}^{-1}$ (at 695 K).

Sodium halides with the UCl_3 -type structure, which can also be formulated as $[\square(\text{M}_2\text{Cl}_6)]$, were also investigated as Na^+ -ion conductors. This hexagonal structure with the space group $P6_3/m$, is formed by the *hcp* arrangement of MX_3 units (Figure 1b).^[46] The empty channels along the [001] direction can be filled by monovalent cations. In addition, cation substitution is also possible, leading to the formation of derivatives with the general formula of $\text{A}'(\text{B}''\text{M}''')\text{X}_6$. In 1998, Meyer et al. successfully synthesized a series of $\text{A}'(\text{B}''\text{M}''')\text{X}_6$ phases, including $\text{Na}(\text{SrSm})\text{Cl}_6$ and $\text{Na}(\text{BaLa})\text{Br}_6$.^[47] The ionic conductivities of the two sodium halides at 300 °C are reported as $\sigma(\text{Na}^+) = 2.81 \cdot 10^{-5} \text{ S cm}^{-1}$ and $\sigma(\text{Na}^+) = 1.12 \cdot 10^{-4} \text{ S cm}^{-1}$, respectively, with a similar activation energy of $E_a = 0.4 \text{ eV}$.



Zhixuan Wei is a post-doctoral researcher in Professor Jürgen Janek's research group in Justus-Liebig-University Giessen, Germany. Her research interests focus on the investigation of solid electrolyte materials for post-lithium solid state batteries. She obtained her Ph.D. degree from Jilin University, China, focusing on the study of energy storage properties of electrodes in non-aqueous and aqueous batteries, with part of research completed at Oregon State University.



Professor Linda Nazar received her B.Sc. in Chemistry from the University of British Columbia in Vancouver, Canada, her Ph.D. in Chemistry from the University of Toronto, and was a postdoctoral fellow at the Exxon Research Labs in Annandale, N.J. She joined the faculty at the University of Waterloo, Ontario, Canada where she is a Chemistry professor, Senior Canada Research Chair in Solid State Energy Materials and Distinguished Research Professor. Nazar is known for her research on electrochemical energy storage with topics that span Li-ion batteries and beyond Li-ion, and solid state ionics.



Jürgen Janek holds a chair for physical chemistry at Justus-Liebig-University in Gießen (Germany) and is scientific director of BELLA, a joint lab of BASF SE and KIT in Karlsruhe/Germany. He received his doctoral degree in physical chemistry, was visiting professor at Seoul National University, Tohoku University, and Université d'Aix-Marseille, and he has received an honorary doctorate from TU Delft. His research spans a wide range from transport studies in mixed conductors and at interfaces to *in situ* studies in electrochemical cells. Current key interests include solid-state batteries, solid electrolytes, and solid electrolyte interfaces. He is particularly interested in kinetics at interfaces.

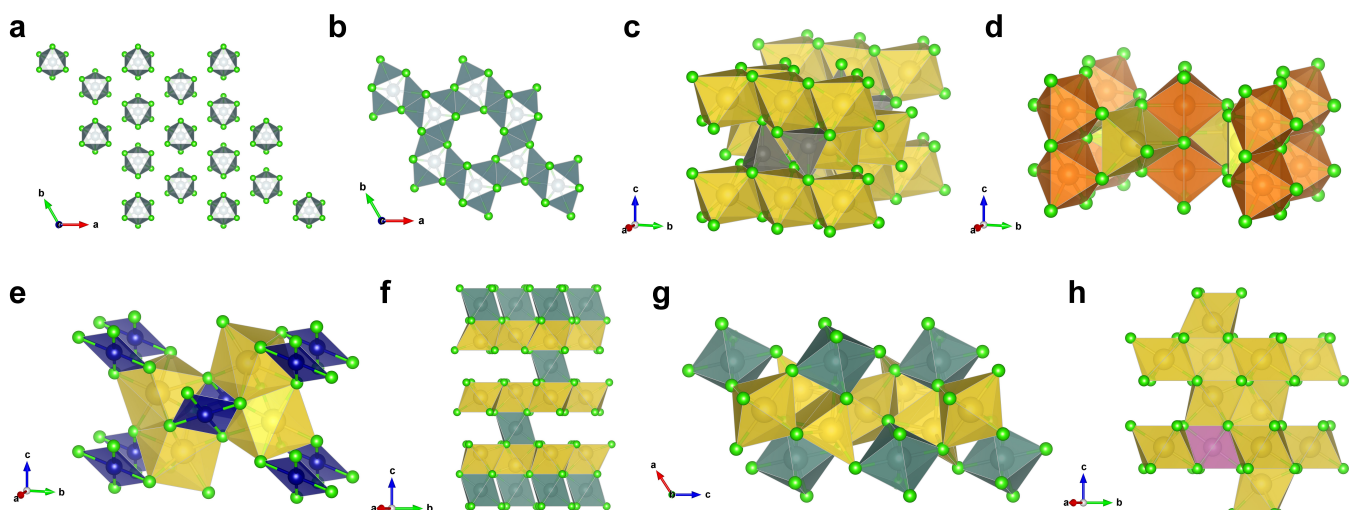


Figure 1. Crystal structure of Na^+ -ion conducting phases: (a) UCl_6 -type (trigonal $\text{P}\bar{3}\text{m}1$); (b) UCl_3 -type (hexagonal $\text{P}6_3/\text{m}$); (c) Na_2ZnCl_4 (orthorhombic Pnma); (d) Na_2MgCl_4 (orthorhombic Pbam); (e) Na_2CrCl_4 (monoclinic $\text{P}2_1/\text{c}$); (f) Na_3YCl_6 (trigonal $\text{R}3$); (g) Na_3YCl_6 (monoclinic $\text{P}2_1/\text{c}$); (h) Na_3InCl_6 (trigonal $\text{P}31\text{c}$). (cif. files from Materials Project; sodium polyhedra are marked in yellow).

2.2. Na_2XCl_4 ($\text{X} = \text{Mg, Ti, Cr, Mn, Co, Zn, Cd}$)

Inspired by fast lithium-ion conductors with a spinel structure ($\text{Li}[\text{LiM}] \text{Cl}_4$, $\text{M} = \text{Mg, Ti, V, Cr, Mn, Fe, Co and Cd}$), Lutz et al. studied the structure and ionic conductivity of their sodium analogues with the formula Na_2XCl_4 .^[48] The structures of the as-prepared powder materials vary depending on the size of the center metal cation. Specifically, Na_2ZnCl_4 and Na_2CoCl_4 exhibit olivine-type structures (Figure 1c), whereas Na_2MgCl_4 , Na_2MnCl_4 and Na_2CdCl_4 show the Sr_2PbO_4 -type structure (Figure 1d); the structure of Na_2CrCl_4 is close to Sr_2PbO_4 but with a monoclinic distortion (Na_2CuF_4 type, Figure 1e). The ionic conductivity improves somewhat with the increase in ionic radius of the metal ion (in the order of $\text{Na}_2\text{MgCl}_4 < \text{Na}_2\text{MnCl}_4 < \text{Na}_2\text{CdCl}_4$), which can be attributed to the decrease in lattice energy. However, the ionic conductivities of all of the above materials are within the range of $\sigma(\text{Na}^+) = 10^{-6} \text{ S cm}^{-1}$ to $10^{-5} \text{ S cm}^{-1}$ at 300°C , being a factor of 10^2 S cm^{-1} lower compared to the Li_2MCl_4 spinels.

Later investigations by Kanno et al. corroborated the above results.^[49] They also concluded that the trend in the ionic conductivity of the olivine-type phase depends on the ionic radius of the central metal ion. The key descriptor appears to be the average $\text{Na}-\text{Cl}$ bond length. The longer the $\text{Na}-\text{Cl}$ bond, the lower the activation energy and, simultaneously, the higher the ionic conductivity (in the order of $\text{Mg} < \text{Mn} < \text{Cd}$). Furthermore, the authors confirmed the lattice distortion in Na_2CrCl_4 by analyzing the structure of solid solutions between monoclinic Na_2CrCl_4 and orthorhombic Na_2MnCl_4 . The $\text{Na}_2(\text{Cr}_{1-x}\text{Mn}_x)\text{Cl}_4$ phases show a continuous monophasic peak shift within the solid-solution range. The lattice distortion can be attributed to the Jahn-Teller effect of the Cr^{2+} ion, which is in the high-spin configuration d^4 state. As a result, the CrCl_6 octahedra are elongated, leading to the transformation from orthorhombic to monoclinic symmetry. On the other hand, the Jahn-Teller effect of the Cr^{2+} ion also causes a distortion in the NaCl_6 trigonal

faces. The non-uniform lengths of the $\text{Na}-\text{Cl}$ bonds block Na^+ ion diffusion, leading to increased activation energy and depressed ionic conductivity of Na_2CrCl_4 .

2.3. Na_3MCl_6 ($\text{M} = \text{Y, In}$)

In 1993, Meyer et al. reported two phases of Na_3YCl_6 in their investigation of $\text{Ag}_{3-x}\text{Na}_x\text{YCl}_6$ solid solutions.^[50] A trigonal $\text{R}3$ phase is observed at lower temperature (Figure 1f), while at 243 K , a phase transition to the monoclinic $\text{P}2_1/n$ structure takes place (Figure 1g). By slowly cooling a melt of binary precursors, the Na_3YCl_6 phase ($\text{P}2_1/n$) was synthesized. The ionic conductivity of this end member phase is $\sigma(\text{Na}^+) = 1 \cdot 10^{-6} \text{ S cm}^{-1}$ at 500 K , which is lower compared to Ag_3YCl_6 ($\sigma(\text{Ag}^+) = 6 \cdot 10^{-4} \text{ S cm}^{-1}$ at 500 K). Na_3InCl_6 was first reported in 1992, which appears to be an incongruously melting compound.^[51] Later in 2005, Yamada et al. successfully prepared single crystals of Na_3InCl_6 and carried out X-ray diffraction (XRD) as well as nuclear magnetic resonance (NMR) spectroscopy to analyze the Na^+ ion conduction mechanism.^[52] At 200 K , the crystal structure of Na_3InCl_6 is trigonal ($\text{P}31\text{c}$) with an *hcp* anion sublattice (Figure 1h). The Na^+ ions sit in two crystallographic sites, octahedrally coordinated by Cl^- . These lead to distinct resonances in the ^{23}Na NMR spectra at 300 K but coalesce at 400 K , suggesting they undergo dynamic chemical exchange through a newly formed Na site. The ionic conductivity at 400 K is around $\sigma(\text{Na}^+) = 1 \cdot 10^{-7} \text{ S cm}^{-1}$, with an activation energy of $E_a = 70.9(5) \text{ kJ mol}^{-1}$.

2.4. Anti-Perovskite Na_3OX ($\text{X} = \text{Cl, Br, I}$)

Encouraged by the high-temperature F^- superionic conductivity in NaMgF_3 perovskite,^[53] lithium-rich anti-perovskites with general formula of Li_3OX have been explored as solid electrolyte materials.^[54–56] These show low electronic conductivity and

enhanced electrochemical stability.^[11,57] Moreover, the simple structure provides plenty of possibilities for ion substitution to tailor properties. Shortly after high lithium-ion conductivity in anti-perovskites was discovered, their sodium analogues were also explored.^[58–64] Wang et al. first reported the synthesis of Na_3OX ($\text{X}=\text{Cl}, \text{Br}, \text{I}$) solid solutions in 2015.^[58] By introducing size-mismatch substitution, a maximum ionic conductivity of $\sigma(\text{Na}^+)=2.3 \cdot 10^{-4} \text{ Scm}^{-1}$ was observed at 180°C , with the composition of $\text{Na}_3\text{OBr}_{0.6}\text{I}_{0.4}$. Based on this stoichiometry, divalent Sr^{2+} ion doping can further boost the conductivity to $\sigma(\text{Na}^+)=9.5 \cdot 10^{-4} \text{ Scm}^{-1}$, with an activation energy of $E_a=0.62 \text{ eV}$. Meng's group pointed out that the synthesis protocol shows significant impact on the local microstructure of Na_3OBr .^[59] Through spark plasma sintering, the particle contact can be improved compared to cold-pressing. Nevertheless, the bulk ionic conductivity of Na_3OBr is in the order of 10^{-7} Scm^{-1} at 180°C , regardless of the processing technique. Zhu et al. reported a conductivity of $\sigma(\text{Na}^+)=1.6 \cdot 10^{-5} \text{ Scm}^{-1}$ at 150°C .^[60] Using *in situ* neutron diffraction, they observed that Na^+ ions hop between NaO_6 octahedra, while Br^- anions are not involved. In the tetragonal modified layered Na_4Ol_2 anti-perovskite, I^- ions bridge the Na^+ hopping pathways in the *c*-axis direction, giving rise to a slightly lower activation energy $E_a=0.30 \text{ eV}$ compared to Na_3OBr ($E_a=0.34 \text{ eV}$).

First-principle calculations were also carried out to predict the properties of anti-perovskites. Ciucci et al. studied the properties of Na_3OCl .^[61] Their results suggested that Na^+ ion migration is enabled by a vacancy hopping mechanism. Hence, generating vacancies by alkaline earth element substitution could be beneficial for the improvement of ionic conductivity, and Ca^{2+} was suggested to be the best candidate. However, the RT conductivity of $\text{Na}_{2.75}\text{Ca}_{0.125}\text{OCl}$ was predicted to be only on the order of 10^{-9} Scm^{-1} . Encouragingly, Jena et al. predicted that by introducing the cluster ion BCl_4^- , a RT Na-ion conductivity of 2.8 mScm^{-1} can be achieved with a very low activation energy of $E_a=0.17 \text{ eV}$ for $\text{Na}_3\text{S}(\text{BCl}_4)$.^[62] The dramatic onset of high ionic conductivity was ascribed to librational motion of the ion clusters, which can smooth out the potential energy landscape and reduce the barrier for ion migration. Nevertheless, no experimental data have been reported to validate this finding to date.

3. Na Halide Solid Electrolyte for Room-Temperature Sodium Solid-State Batteries

In recent years, the successful application of lithium metal halide-based electrolyte in solid-state lithium batteries has stimulated the exploration of their sodium analogues. Moreover, the development of materials synthesis and characterization techniques in the last two decades provides new platforms for a deeper understanding of the properties and performance of SE materials. In this section, we introduce several successful examples of Na metal halide SEs that have been synthesized and utilized as separators in solid-state

sodium batteries. This includes discussion of synthesis-structure-property correlations, and the electrochemical performance of practical cells.

3.1. Monoclinic Na_3MCl_6 ($\text{M}=\text{Er}, \text{Y}$)

3.1.1. Zr-Modified Na_3ErCl_6 Solid Solutions ($\text{Na}_{3-x}\text{Er}_{1-x}\text{Zr}_x\text{Cl}_6$)

In 2020, Zeier's group prepared a series of $\text{Na}_{3-x}\text{Er}_{1-x}\text{Zr}_x\text{Cl}_6$ solid solutions and studied the structural evolution invoked by substituting Zr^{4+} for Er^{3+} .^[36] The end members, i.e., Na_3ErCl_6 and Na_2ZrCl_6 , crystallize in a monoclinic ($P2_1/n$) and trigonal ($P\bar{3}m1$) space group, respectively. Na_3ErCl_6 exhibits a perfect close-packed structure of ErCl_6 octahedra with Na in all octahedral and tetrahedral sites, where the fully occupied sodium polyhedra leave no vacancies for mobile sodium ions to hop into, leading to poor ionic conductivities. On the other hand, the NaCl_6 octahedra in Na_2ZrCl_6 form a honeycomb-like lattice by edge-sharing in the *ab*-plane. By substituting Er^{3+} by Zr^{4+} , additional vacancies are introduced into the structure of Na_3ErCl_6 to maintain charge balance. Rietveld refinement of the XRD data reveals the structural changes upon introducing Zr^{4+} . As shown in Figure 2a and 2b, the $\text{Na}_{3-x}\text{Er}_{1-x}\text{Zr}_x\text{Cl}_6$ solid solution adopts the monoclinic structure of Na_3ErCl_6 , and the lattice parameters decrease with increasing Zr^{4+} substitution due to its smaller ionic radius. Nevertheless, the decrease is not linear (Figure 2c–f). For $x(\text{Zr})>0.6$, changes in the polyhedra takes place, characterized by halide ion repositioning and distortion of the polyhedra, until the trigonal endmember Na_2ZrCl_6 is reached. Along with the local structure rearrangement, the ionic conductivity increases as a result of introducing vacancies into the lattice, from $\sigma(\text{Na}^+)=10^{-6} \text{ mScm}^{-1}$ (Na_3ErCl_6) to a maximum of $\sigma(\text{Na}^+)=0.035 \text{ mScm}^{-1}$ ($\text{Na}_{2.4}\text{Er}_{0.4}\text{Zr}_{0.6}\text{Cl}_6$). A bond-valence-sum analysis was carried out to visualize the Na^+ diffusion pathways. In $\text{Na}_{2.4}\text{Er}_{0.4}\text{Zr}_{0.6}\text{Cl}_6$, three diffusion pathways are possible, including *oct-prismatic*, *oct-i1-i2-prismatic* and *oct-i3-oct*, respectively (Figure 2g–i). The occupancy of the interstitial sites could not be resolved by Rietveld refinement, which indicates that they are probably short-lived intermediate states. This leads to overall activation barriers for Na^+ ion diffusion between $E_a=0.4$ and 0.6 eV . These promising results provide a platform for further experimental investigation on halide-based SE materials for sodium-ion conduction.

3.1.2. Zr-Modified Na_3YCl_6 Solid Solutions ($\text{Na}_{3-x}\text{Y}_{1-x}\text{Zr}_x\text{Cl}_6$)

Owing to its low dopant formation energy, Zr^{4+} has also been introduced into Na_3YCl_6 ,^[37] which crystallizes in a monoclinic lattice ($P2_1/n$). Unlike its lithium analogue that crystallizes in the trigonal $P\bar{3}m1$ space group,^[30] Na_3YCl_6 has a much lower RT ionic conductivity, which is attributed to the full occupancy of the *2d* and *4e* Na sites in the lattice. Upon doping by Zr^{4+} , the crystal structure of Na_3YCl_6 is maintained within the solid solution limit ($x<0.875$), as shown in Figure 3a. The ionic conductivity of the doped material shows the highest value of

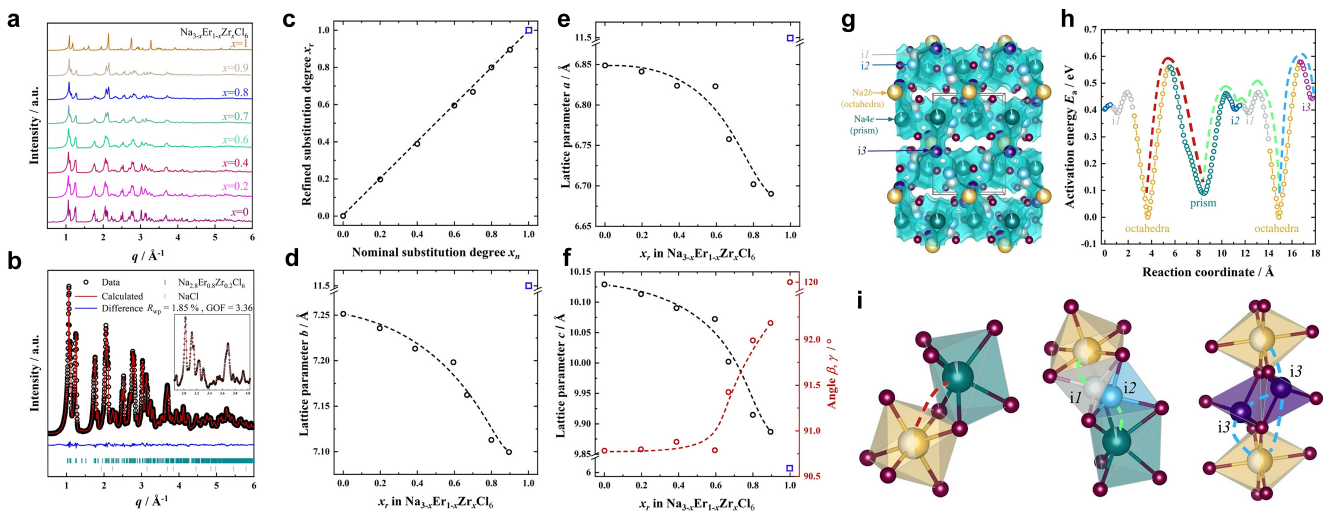


Figure 2. Structural change as function of Zr substitution: (a) comparison of the collected XRD patterns with (b) showing exemplary Rietveld refinement of $\text{Na}_{3.8}\text{Er}_{0.8}\text{Zr}_{0.2}\text{Cl}_6$; (c) refined Zr^{4+} content vs nominal Zr^{4+} content showing no visible solubility limit; (d–f) change in lattice parameters. Na^+ ion pathways: (g) lowest energy bond-valence landscape showing the preferred sodium diffusion trajectory; (h) potential landscape of $\text{Na}_{3.8}\text{Er}_{0.8}\text{Zr}_{0.2}\text{Cl}_6$ with three different diffusion mechanisms with colored pathways shown in (i). Reproduced with permission.^[36] Copyright © 2020, American Chemical Society.

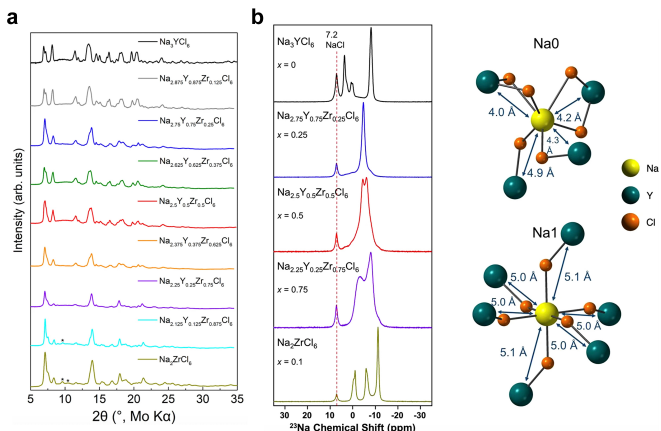


Figure 3. Structural characterization of $\text{Na}_{3-x}\text{Y}_{1-x}\text{Zr}_x\text{Cl}_6$: (a) XRD patterns; (b) ^{23}Na single-pulse solid-state NMR spectra and schematic of the Na0 and Na1 local environments in Na_3YCl_6 . Reproduced under terms of the CC-BY 4.0 license.^[37] Copyright © 2021, E. A. Wu et al., Nat. Commun. 2021, published by Springer Nature.

$\sigma(\text{Na}^+, \text{RT}) = 6.6 \cdot 10^{-5} \text{ S cm}^{-1}$ at a composition of $\text{Na}_{2.125}\text{Y}_{0.125}\text{Zr}_{0.875}\text{Cl}_6$. Above that Zr content, crystalline Na_2ZrCl_6 exsolves as a second phase, leading to a drop in ionic conductivity. Magic angle spinning (MAS) solid-state NMR spectra of ^{23}Na also suggest facilitated Na^+ diffusion in the doped samples. Specifically, the spectrum of Na_3YCl_6 exhibits more than five distinct resonances (Figure 3b), which unfortunately cannot be fully assigned. Nevertheless, upon the substitution of Y by Zr, the signals coalesce into single or double dominant peaks. This indicates fast chemical exchange on the experimental timescale in the Na local environments, suggestive of fast Na^+ diffusion. Moreover, *ab initio* molecular dynamics (AIMD) simulations at 600 K suggest that due to the cell volume expansion upon Zr^{4+} doping, $\text{YCl}_6^{3-}/\text{ZrCl}_6^{2-}$ octahedral rotation is triggered (at $x=0.75$). On the other hand, the Cl^- ions in Na_3YCl_6 remain relatively static. Counter-intuitively,

partial substitution of the rare earth ion by Zr^{4+} which has a smaller ionic radius results in lattice expansion of Na_3YCl_6 (unlike the lattice shrinkage of isostructural Na_3ErCl_6 , as discussed in the last section). In a gedankenexperiment, the octahedra in $\text{Na}_{2.25}\text{Y}_{0.25}\text{Zr}_{0.75}\text{Cl}_6$ were frozen at their initial position (at 800 K). As a result, the Na^+ mobility displays no significant difference compared to the undoped Na_3YCl_6 , in spite of the increased cell volume. Therefore, it is suggested that the polyanion rotation plays a significant role in enhancing the Na^+ ionic conductivity of $\text{Na}_{2.25}\text{Y}_{0.25}\text{Zr}_{0.75}\text{Cl}_6$. Note that the increase of cell volume due to the Zr^{4+} doping is indispensable. In another gedankenexperiment, the cell volume of $\text{Na}_{2.25}\text{Y}_{0.25}\text{Zr}_{0.75}\text{Cl}_6$ is constrained to the same value as Na_3YCl_6 . Consequently, the octahedral rotation sharply decreases, so as the ionic conductivity.

Typical of the halides, Zr-doped Na_3YCl_6 exhibits a high oxidation limit (up to 3.8 V vs. Na^+/Na). This provides the opportunity to use a high-voltage layered phase, e.g., NaCrO_2 , as a cathode material to build a model SSSB. In this configuration, a Na–Sn alloy and Na_3PS_4 were used as anode and separator electrolyte, respectively, and a composite of NaCrO_2 , $\text{Na}_{2.25}\text{Y}_{0.25}\text{Zr}_{0.75}\text{Cl}_6$ catholyte and conductive carbon was used as the cathode (Figure 4a). At 40 °C, the ionic conductivity of $\text{Na}_{2.25}\text{Y}_{0.25}\text{Zr}_{0.75}\text{Cl}_6$ increased to $\sigma(\text{Na}^+) \sim 1.5 \cdot 10^{-4} \text{ S cm}^{-1}$. As a result of the enhanced kinetics, the model SSSB cell exhibited reversible capacity of $78 \text{ mAh g}_{\text{NaCrO}_2}^{-1}$ at a 1 C rate (current density of 0.64 mA cm^{-2}), with a high capacity retention of 89.3% after cycling over 1000 cycles (Figure 4b). Post-mortem high-resolution X-ray photoelectron spectra (XPS) suggest that the Zr–Cl and Y–Cl bonds in the Zr 3d and Y 3d XP spectra are both retained, indicating the good electrochemical stability of $\text{Na}_{2.25}\text{Y}_{0.25}\text{Zr}_{0.75}\text{Cl}_6$ (Figure 4c–d). The results mark an important step forward towards the application of halide Na-ion conductors in full battery cells. However, the subpar conductivity of

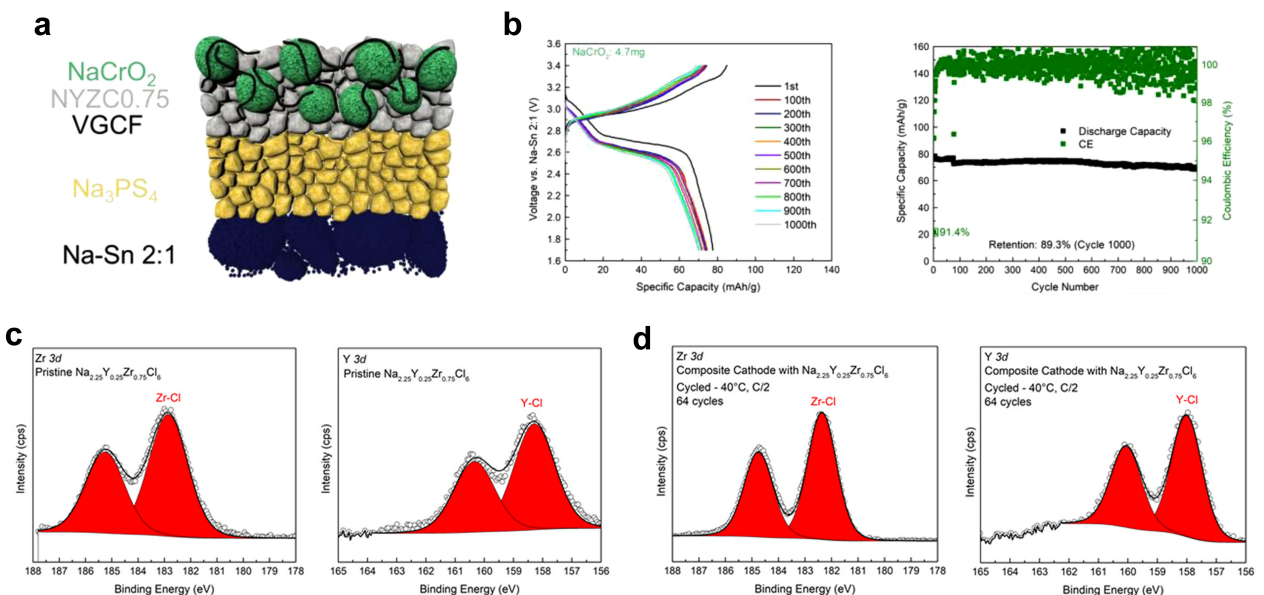


Figure 4. Electrochemical performance of SSSBs using NYZC0.75 as catholyte: (a) scheme of cell configuration; (b) voltage profile and specific capacity as a function of cycle number for cells at 40 °C at a 1 C rate; XPS spectra (c) before and (d) after cycling. Reproduced under terms of the CC-BY 4.0 license.^[37] Copyright © 2021, E. A. Wu et al., Nat. Commun. 2021, published by Springer Nature.

the SE limits the thickness of the cathode composite and the energy density of the full cells.

The synthesis parameters also have a significant effect on the ionic transport behavior of the Na-Y-Zr-Cl solid solutions. To understand the governing factors, the group of Clément carried out follow-up studies on $\text{Na}_{3-x}\text{Y}_{1-x}\text{Zr}_x\text{Cl}_6$ to systematically investigate the synthetic control of structure in this series, and the corresponding impact on ion conduction properties.^[38] To prepare one of the end members, Na_2ZrCl_6 , the precursors were mechanochemically mixed, followed by an annealing step at 500 °C for 24 h. The samples were then processed by three different methods, including slow cooling, quenching in a water bath, and ball-milling again after quenching. Interestingly, the slow-cooled sample exhibited a single $\bar{P}3m1$ phase in the XRD pattern, while a small amount of a $P2_1/n$ phase emerged in the quenched sample, which became the dominant phase after the second ball-milling process. Density functional theory (DFT) calculations unravelled the underlying reason: the $\bar{P}3m1$ phase is thermodynamically stable, so not prone to decompose into the NaCl and ZrCl_4 binary compounds, while the $P2_1/n$ polymorph is metastable, exhibiting an E_{hull} of 17 meV atom⁻¹, and can only be obtained via non-equilibrium synthesis approaches. In addition, ²³Na ss-NMR spectra suggest that the second ball-milling process increased the disorder on the cation lattice. This could be attributed to either the population of additional Zr sites or the generation of stacking faults.^[35,65] As a result, additional Na local environments were generated. The fraction of the $P2_1/n$ phase is in line with the RT ionic conductivity, increasing from $\sigma(\text{Na}^+)=6.6 \cdot 10^{-8} \text{ Scm}^{-1}$ (slow-cooled) to $\sigma(\text{Na}^+)=2.6 \cdot 10^{-5} \text{ Scm}^{-1}$ (second ball-milled). Variable temperature ²³Na ss-NMR also suggests faster Na^+ ion hopping between prismatic sites in the $P2_1/n$ structure. In sharp contrast, the Na^+ ion hopping rate between the two sites in the

$\bar{P}3m1$ structure is much lower, indicative of the poorly ion-conducting behavior.

The other end member, Na_3YCl_6 , was investigated by the same methods, which also shows two polymorphs adopting $R\bar{3}$ and $P2_1/n$ symmetry, respectively. Similarly, the $R\bar{3}$ phase obtained by slow cooling is thermodynamically stable, while the $P2_1/n$ phase in the quenched (as well as the second ball-milled) sample is slightly metastable, with an E_{hull} of 8.8 meV atom⁻¹. Unlike Na_2ZrCl_6 , the second ball-milling process does not alter the phase. Moreover, the ionic conductivities of the three Na_3YCl_6 samples follow the same trend as Na_2ZrCl_6 . Specifically, the conductivities of quenched and subsequently ball-milled samples are $\sigma(\text{Na}^+)=1.6 \cdot 10^{-11} \text{ Scm}^{-1}$ and $\sigma(\text{Na}^+)=9.5 \cdot 10^{-8} \text{ Scm}^{-1}$ at 60 °C and 25 °C, respectively, while the $R\bar{3}$ phase sample shows no detectable ionic conductivity even at 60 °C. The much lower ionic conductivity of Na_3YCl_6 compared to Na_2ZrCl_6 could be attributed to the completely filled Na sites caused by stuffing Na into the lattice, which drastically limits the Na^+ ion migration. Additionally, the isotropic hopping pathway for Na^+ ions in the $P2_1/n$ phase further increases the conductivity relative to the anisotropic hopping pathway in $\bar{P}3m1$ structured Na_2ZrCl_6 . The above results point out that, for the design of Na halides with enhanced ionic conductivity, it is key to introduce intrinsic cation vacancies, and to create isotropic conduction pathways.

To gain further understanding on the correlations between structure and ion transport properties, $\text{Na}_{2.25}\text{Y}_{0.25}\text{Zr}_{0.75}\text{Cl}_6$ was prepared by different routes. Through slow cooling, a $P2_1/n$ phase was obtained. However, the RT ionic conductivities follow the same trend as the parent materials Na_2ZrCl_6 and Na_3YCl_6 , which are $\sigma(\text{Na}^+)=9.5 \cdot 10^{-6} \text{ Scm}^{-1}$, $\sigma(\text{Na}^+)=1.3 \cdot 10^{-5} \text{ Scm}^{-1}$ and $\sigma(\text{Na}^+)=6.6 \cdot 10^{-5} \text{ Scm}^{-1}$ for the slow cooled, quenched and second ball-milled samples, respectively. Evaluation of the

structure indicates that the transition metal (TM) species are in a layered configuration in the ground state structure, while Na ions occupy 100% of the prismatic sites and 25% of the octahedral sites. Molecular dynamics (MD) simulations were carried out to understand the impact of Na-vac and Y-Zr disorder on the ionic conduction properties. The results suggest that varying the Na occupancy causes a minimal effect on the ion diffusion with respect to activation energy and ionic conductivity. However, the double ball-milling process introduces more Y-Zr mixing, which significantly improved Na diffusion. The TM mixing was also found to promote Na site disorder, as well as partially activate Cl vibrational modes, which, according to previous studies, also promotes Na ion mobility.^[36] This work reveals the significance of post-sintering parameters on the polymorph formation of Na halide materials, as well as the subsequent effect on ion transport, which contributes to the understanding of synthesis-structure-property correlations. Further investigations on other determining parameters, including crystallinity, degree of disorder, etc., are clearly indispensable for the guidance of designing superionic conducting Na halides.

3.2. Trigonal Na_2ZrCl_6

3.2.1. Na_2ZrCl_6

Jung's group reported the synthesis of Na_2ZrCl_6 and its application in SSSBs.^[40] After ball-milling (BM), BM- Na_2ZrCl_6 exhibits an ionic conductivity of $\sigma(\text{Na}^+) = 1.8 \cdot 10^{-5} \text{ S cm}^{-1}$ (30 °C), with an activation energy of $E_a = 0.4 \text{ eV}$. After high-temperature treatment, the crystal structure of Na_2ZrCl_6 is retained (trigonal structure with $P\bar{3}m1$ symmetry), as suggested by Rietveld refinement (Figure 5). With the crystallinity increasing, the ionic conductivity drops strongly to $\sigma(\text{Na}^+) = 6.9 \cdot 10^{-8} \text{ S cm}^{-1}$. Compared to isostructural trigonal Li_3ErCl_6 ,^[34] which shows two Wyckoff sites that Li ions occupy (fully on the 6g and half on

the 6h site), the low conductivity of the well-crystallized HT- Na_2ZrCl_6 phase could be attributed to the strong bonding between Na^+ and Cl^- in the lattice, as well as the absence of a partially populated 6h interstitial site. With mechanochemical-milling, disorder is introduced on both the M and Na^+ sites, which results in partial occupation of interstitial Na sites as well as rearrangement of Na^+ channels. The flattened energy landscape provides facilitated Na^+ migration pathways, and increases the Na^+ -ion conductivity.

Electrochemical characterization was also carried out to evaluate the potential application of BM- Na_2ZrCl_6 . Remarkably, excellent oxidation stability was observed up to 5 V (vs. Na^+/Na). SSSB cells using a Na_3Sn anode, Na_3PS_4 separator electrolyte and a $\text{NaCrO}_2/\text{BM-Na}_2\text{ZrCl}_6$ cathode composite showed a reversible capacity of $111 \text{ mAh g}_{\text{NaCrO}_2}^{-1}$ and a high initial Coulomb efficiency of 93.1% at 0.1 C (12 mAg $_{\text{NaCrO}_2}^{-1}$), outperforming counterpart SSSB cells using Na_3PS_4 as the catholyte, which exhibit a reversible capacity of only $90 \text{ mAh g}_{\text{NaCrO}_2}^{-1}$. EIS studies, along with *ex situ* XPS characterization also suggest good interfacial stability between the cathode composite and the separator electrolyte up to 3.6 V. Based on the promising electrochemical performance of the SSSB, further improvement at the cell-level is expected upon enhancing the ionic conductivity of Na_2ZrCl_6 via alio- and/or iso-valent atom substitution.

The ionic conductivity of Na_2ZrCl_6 was further increased by incorporating ZrO_2 nanoparticles to generate percolating interfaces. Jung's group synthesized nanocomposite SEs of the type $\text{ZrO}_2\text{-}(\text{Cl}-)\text{-A}_2\text{ZrCl}_6$ ($\text{A}=\text{Li}$ or Na) mechanochemically,^[66] which improved the ionic conductivity of A_2ZrCl_6 by one order of magnitude, i.e., from $\sigma(\text{Li}^+, 30^\circ\text{C}) = 0.4 \text{ mS cm}^{-1}$ and $\sigma(\text{Na}^+, 30^\circ\text{C}) = 0.011 \text{ mS cm}^{-1}$ to $\sigma(\text{Li}^+, 30^\circ\text{C}) = 1.3 \text{ mS cm}^{-1}$ and $\sigma(\text{Na}^+, 30^\circ\text{C}) = 0.11 \text{ mS cm}^{-1}$, respectively. Through theoretical simulations and extended X-ray absorption fine structure analysis, the enhanced interfacial conduction for Li^+ was attributed to some anion exchange between ZrO_2 and Li_2ZrCl_6 nanodomains. The interphase – assumed to be $\text{Li}_{2.5}\text{ZrCl}_{5.5}\text{O}_{0.5}$ – offers faster Li^+ ion diffusion compared to Li_2ZrCl_6 . The authors attribute this to the Li enrichment as well as to volume expansion. In a similar way, the increased Na^+ ion conductivity is also attributed to formation of the interphase. The strategy seems generally applicable. By replacing ZrO_2 with SnO_2 , the $\text{SnO}_2\text{-}2\text{Li}_2\text{ZrCl}_6$ composite exhibits an ionic conductivity of $\sigma(\text{Li}^+, 30^\circ\text{C}) = 1.6 \text{ mS cm}^{-1}$; the sodium analog is not reported.

3.2.2. In-Modified Na_2ZrCl_6 Solid Solution ($\text{Na}_{2+x}\text{Zr}_{1-x}\text{In}_x\text{Cl}_6$)

As mentioned before, post-sintering conditions exhibit a significant effect on the polymorph formation of $\text{Na}_{3-x}\text{Y}_{1-x}\text{Zr}_x\text{Cl}_6$. Apart from that, it has also been observed that high-temperature treatment following mechanochemical synthesis has a significant effect on the ion transport properties of lithium halide solid electrolytes.^[30,34,67,68] However, there is still a gap in correlating heating protocol and transport properties for sodium halides. To this end, Zeier's group synthesized a series of solid solutions of $\text{Na}_{2+x}\text{Zr}_{1-x}\text{In}_x\text{Cl}_6$ and investigated how

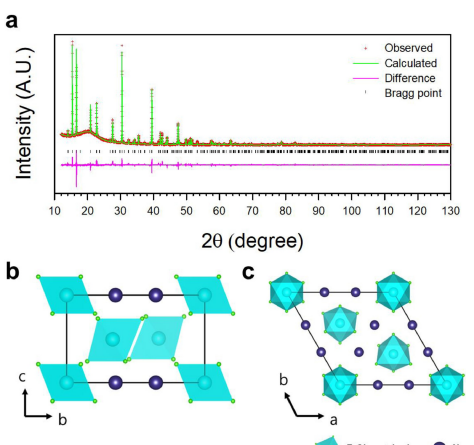


Figure 5. Structural characterization of HT- Na_2ZrCl_6 : a) Rietveld refinement profile for HT- Na_2ZrCl_6 . Crystal structure of Na_2ZrCl_6 , showing b) (100) and c) (001) views where the unit cells are outlined. Reproduced with permission.^[40] Copyright © 2021, Elsevier B.V.

heating parameters affect the crystal structure, and thus regulate ionic transport in halide Na^+ ion conductors.^[39] First of all, it has been observed that the solubility limit of the $\text{Na}_{2+x}\text{Zr}_{1-x}\text{In}_x\text{Cl}_6$ solid solution depends on temperature. At 330 °C, a distinct secondary phase starts to grow when the substitution degree $x(\text{In})$ reaches 0.5. It crystallizes as a trigonal phase ($P\bar{3}c$) which is isostructural to the end member Na_3InCl_6 . To the contrary, all of the solid solutions ($x=0.1\sim0.9$) annealed at 200 °C show the pure $P2_1/n$ monoclinic phase, which is also the structure that cation-mixed sodium halides generally adopt.^[36,37] Besides, the change in cell parameters exhibit two regions with different slopes (Figure 6a). Interestingly, in this case, the solid solution inherits the structure type of neither end member Na_2ZrCl_6 ($P\bar{3}m1$ phase) nor the other end member Na_3InCl_6 ($P\bar{3}1c$ phase). Secondly, the substitution degree also shows impact on the occupancy of Na in NaCl_6^{5-} polyhedra. Interestingly, with the increase in $x(\text{In})$, the occupancy of the $\text{Na}(4e)$ site remains stable at values close to 100%, while the occupancy on the $\text{Na}(2b)$ site exhibits a positive correlation with $x(\text{In})$ (Figure 6b).

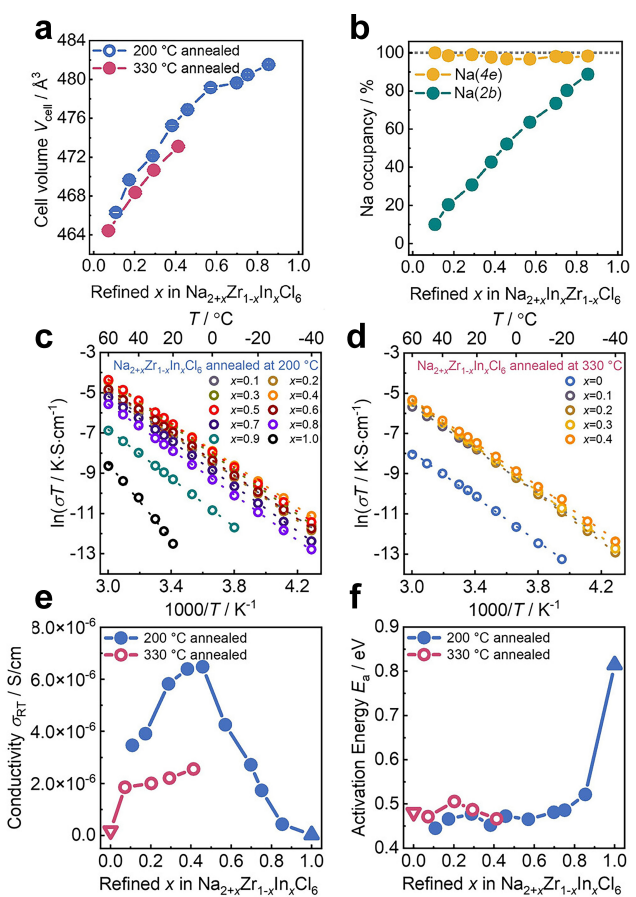


Figure 6. Structural changes as function of temperature and In substitution degree: (a) cell volumes for materials annealed at 200 and 330 °C; (b) Na^+ occupancies on 2b and 4e sites (annealed at 200 °C). Ion conduction behavior as function of temperature and In substitution degree: Arrhenius plots from the temperature-dependent impedance of $\text{Na}_{2+x}\text{Zr}_{1-x}\text{In}_x\text{Cl}_6$ annealed at (c) 200 °C and (d) 330 °C; (e) ionic conductivities and (f) activation energies annealed at 200 and 330 °C. Reproduced with permission.^[39] Copyright © 2023, T. Zhao et al., published by American Chemical Society

The RT ionic conductivity of $\text{Na}_{2+x}\text{Zr}_{1-x}\text{In}_x\text{Cl}_6$ solid solutions exhibit a strong correlation with the structural parameters discussed above. For the materials annealed at 200 °C, the ionic conductivity shows an increasing trend until $x(\text{In})=0.5$, with a maximum value of $\sigma(\text{Na}^+) \sim 6.5 \cdot 10^{-6} \text{ Scm}^{-1}$ (Figure 6c, e). Further increasing the indium content induces a sharp decrease in ionic conductivity, which reaches the lowest value for Na_3InCl_6 ($\sigma(\text{Na}^+) \sim 2.3 \cdot 10^{-8} \text{ Scm}^{-1}$) and the highest activation energy (Figure 6f). In addition, $\text{Na}_{2+x}\text{Zr}_{1-x}\text{In}_x\text{Cl}_6$ annealed at 330 °C also exhibits a positive correlation between ionic conductivity and substitution degree within the solid solution limit ($x=0.1\sim0.4$) (Figure 6d, e). Through the bond valence sum approach, it was concluded that the relative occupancy of the two Na sites play a significant role in ionic transport, especially the unoccupied 2b site. When the occupancy of $\text{Na}(2b)$ is below 60%, the ionic conductivity positively correlates with the $\text{Na}(2b)$ occupancy. Beyond this limit, a negative correlation is observed since the vacancies for Na^+ hopping start to be blocked. This vacancy-conductivity correlation trend is similar in other Na halides, such as $\text{Na}_{2+x}\text{Zr}_{1-x}\text{Y}_x\text{Cl}_6$ and $\text{Na}_{2+x}\text{Zr}_{1-x}\text{Er}_x\text{Cl}_6$. The results shown in this work mark the importance of heat treatment protocol on the solubility of doping ions in Na halides, and unravel the importance of the Na^+ /vacancy ratio, as well as the crystallinity on the ion transport performance.

3.3. Orthorhombic NaAlCl_4

The enhanced ionic conductivity of mechanochemically prepared materials compared to their annealed analogues is also exemplified by a new NaAlCl_4 solid electrolyte.^[41] NaAlCl_4 has been investigated as molten-salt electrolyte in high-temperature Na metal batteries due to its low melting temperature of 160 °C.^[69,70] Recently, Jung's group reported a series of NaAlCl_4 solid electrolytes for SSSBs, with maximum $\sigma(\text{Na}^+) = 3.9 \cdot 10^{-6} \text{ Scm}^{-1}$ at 30 °C, and an activation energy of $E_a = 0.42 \text{ eV}$ (Figure 7a). At 60 °C, the conductivity could be increased to $\sigma(\text{Na}^+) = 1.7 \cdot 10^{-5} \text{ Scm}^{-1}$. NaAlCl_4 crystallized in an orthorhombic $P2_{12}2_1$ structure after mechanochemical milling process (Figure 7b). High-temperature annealing showed no influence on the structure, but notably increased the crystallinity. Due to its small ion radius (50 pm), Al^{3+} forms AlCl_4^- tetrahedra instead of showing octahedral coordination as in Na_3MCl_6 . Na atoms occupy two Wyckoff positions. Rietveld refinement reveals that in the ball-milled materials (BM- NaAlCl_4), Na^+ is positioned on both sites. However, in the heat-treated material (HT200- NaAlCl_4), Na^+ most likely solely occupies the Na1 site. Bond valence energy landscape (BVEL) analyses provide evidence of preferred 1D Na^+ ion migration pathways in BM- NaAlCl_4 . Additionally, the occupation of the Na2 site in this material enhances the connectivity of the Na^+ ion migration pathways, which enhances the Na^+ ion conductivity by 10-fold compared to HT200- NaAlCl_4 ($3.3 \cdot 10^{-7} \text{ Scm}^{-1}$ at 30 °C).

BM- NaAlCl_4 was used as a catholyte to assess the electrochemical performance in SSSB cells. Evaluation of the electrochemical stability window by CV measurements showed that similar to other halide-based SEs, BM- NaAlCl_4 shows high

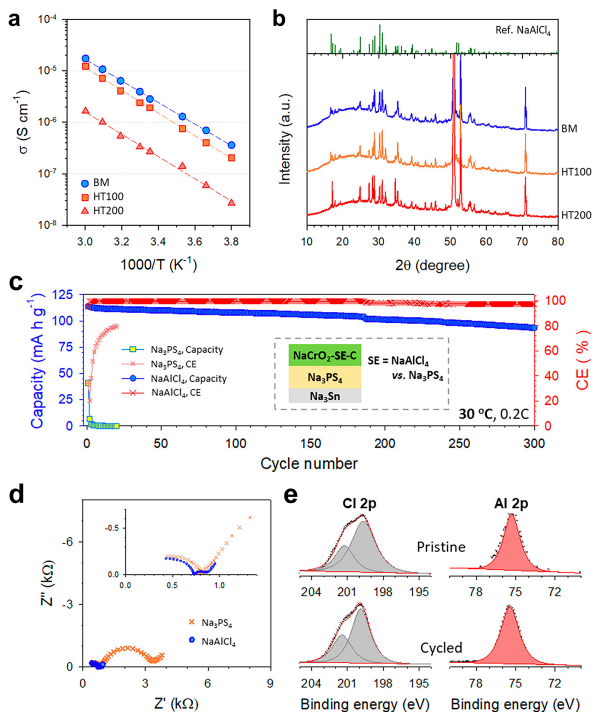


Figure 7. Characterization of BM-, HT100-, and HT200-NaAlCl₄: (a) Arrhenius plots of Na⁺-ion conductivity and (b) powder XRD patterns; Electrochemical performance of SSSBs using NaAlCl₄ as catholyte: (c) cycling performance at 30 °C and 0.2 C for NaCrO₂ electrodes employing BM-NaAlCl₄ or Na₃PS₄ and (d) corresponding Nyquist plots at the first cycle; (e) XPS signals of NaCrO₂ electrodes using BM-NaAlCl₄ before and after 20 cycles at 30 °C. Reproduced with permission.^[41] Copyright © 2022, American Chemical Society.

oxidation stability up to 4.0 V (vs. Na⁺/Na), consistent with their first principles calculations result (4.2 V),^[41] and coupled with poor reduction stability based on an onset potential at 2.0 V. The electrochemical stability in a practical cell was also assessed, using Na_{0.67}Ni_{0.1}Co_{0.1}Mn_{0.8}O₂ (NanCM118) mixed with BM-NaAlCl₄ as the cathode composite. The NanCM118/Na₃Sn SSSB cell was cycled between 2.0 V and an upper cutoff voltage that was increased stepwise from 3.5 V to 4.1 V. At a cutoff voltage of 3.95 V, the SSSB showed a Coulomb efficiency (CE) of nearly 100%, but at 4.1 V the CE of only 16% confirms the 4.0 V oxidation stability limit. A 3 V class SSSB was thus assembled using Na₃PS₄ as separator, NaCrO₂ as the cathode active material, BM-NaAlCl₄ as catholyte and Na₃Sn as anode. At 30 °C and 0.2 C rate (24 mA g_{NaCrO2} $^{-1}$) using constant current-constant voltage charging mode, an initial discharge capacity of 114 mA h g_{NaCrO2} $^{-1}$ was delivered (mass loading of 11.3 mg cm $^{-2}$), with a high capacity retention of 82% after 300 cycles. The electrochemical performance of the full cell significantly outperforms the control experiment using Na₃PS₄ as the catholyte instead of NaAlCl₄, where the former exhibits an initial capacity lower than 50 mA h g $^{-1}$ and loses electrochemical activity from the second cycle (Figure 7c). XP spectra of the cathode composites after cycling demonstrate negligible changes, and the interfacial resistance reflected by the impedance spectra is also sharply decreased compared with the Na₃PS₄ counterpart (Figure 7d-e). Since the ionic conductivity of Na₃PS₄ is two

orders of magnitude higher compared to NaAlCl₄ [$\sigma(\text{Na}^+) = 1.0 \cdot 10^{-4}$ Scm $^{-1}$ compared to $\sigma(\text{Na}^+) = 3.9 \cdot 10^{-6}$ Scm $^{-1}$], clearly interfacial stability is the more critical factor for a functional SSSB cell as such – while the conductivity is essential for the performance of the SSB. It is worth to note that NaAlCl₄ solid electrolytes for SSSBs are well aligned with the overarching goal of developing sodium-based energy storage systems, since all of the elements are cost-effective and highly abundant. However, halide SE materials with higher ionic conductivity still need to be developed to further enhance the electrochemical properties of SSSBs.

3.4. Amorphous Materials

In contrast to crystalline phases with long-range ordered lattices, amorphous materials are constructed by atom clusters randomly connected to each other, resulting only in short-range order. As a result, they can exhibit weakened bonding between charge carriers and the supporting matrix, as well as good mechanical properties. This year, Sun's group reported an amorphous NaTaCl₆ halide SE,^[42] with an impressive ionic conductivity of $\sigma(\text{Na}^+) = 4 \cdot 10^{-3}$ Scm $^{-1}$ at RT, much higher than its crystalline form after annealing ($\sim 10^{-6}$ Scm $^{-1}$). The crystalline NaTaCl₆ is isostructural to Na₃YCl₆, with a monoclinic structure and P2₁/n space group. Defects can be easily introduced during high-energy ball milling (including oxygen, although this was not discussed). As shown in the schematic (Figure 8a), after ball-milling, the Na-Cl interaction is claimed to be weakened, and a poly-(TaCl₆)-octahedral network forms, via rearrangement and distortion of TaCl₆ octahedra. The poly-(TaCl₆) backbone apparently "repels" Na⁺ ions to the amorphous halide matrix by electrostatic forces, which facilitates Na⁺-ion migration". This merits further study. Electrochemical characterization shows that amorphous NaTaCl₆ SE exhibits a stability window from 2.5 to 4.0 V (vs. Na⁺/Na₁₅Sn₄). Using Na₃V₂(PO₄)₃ (denoted as NVP) as the cathode active material, the Na₁₅Sn₄|Na₃PS₄|NaTaCl₆|NVP/NaTaCl₆ cell delivered a discharge capacity of 111 mA h g_{NVP} $^{-1}$ at a rate of 0.1C. The initial Coulomb efficiency achieved was 99.6%, which can be attributed to a good match with the working potential of NVP, as well as its good chemical

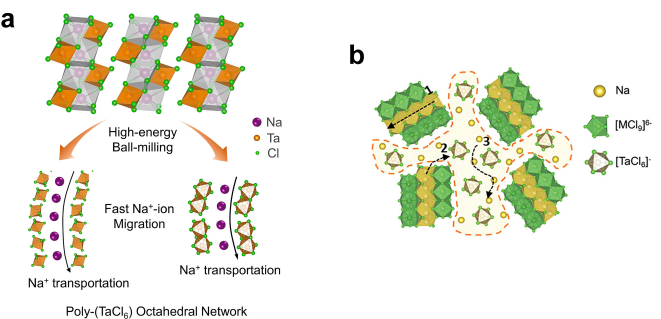


Figure 8. Illustration of Na⁺-ion migration pathways: (a) Na-ion conduction mechanism in amorphous NaTaCl₆. Reproduced with permission.^[42] Copyright © 2023, Elsevier Inc; (b) the schematic diagram of heterogeneous halide composites. Reproduced with permission.^[72] Copyright © 2023, J. Fu et al., Wiley-VCH.

compatibility with the halide SE. The reported cells also exhibited superior rate performance and long cycle stability. At a 1C rate (areal current density of 0.46 mA cm^{-2}), the capacity retention reached 95% after 600 cycles. Due to the plasticity of the amorphous SE, the cathode composite appears to be mechanically quite stable.

This year, Hayashi et al. also reported on the preparation of NaTaCl_6 using a mechanochemical method. The microstructure of the as-prepared material is composed of NaTaCl_6 nanocrystals dispersed into an amorphous matrix. The material exhibits an ionic conductivity of $\sigma(\text{Na}^+) = 6.2 \cdot 10^{-5} \text{ S cm}^{-1}$ at 25°C , with activation energy of 0.37 eV, again suggesting the potential of NaTaCl_6 as an "end-member" of chloride electrolytes.^[71] We like to emphasize that amorphization through ball milling always bears the risk of unintentional doping with the milling media. Yet these recent reports are highly promising.

3.5. Heterogeneous Materials

Very recently, Sun's group reported a heterogeneous halide SE, which combines an amorphous low-coordination phase with a crystallized UCl_3 -type high-coordination framework.^[72] Specifically, the C.N. of cations is determined by the cation:anion radius ratio according to Pauling's rules for ionic compounds. In the high-coordination framework ($\text{C.N.} > 6$) of $\text{Na}_{0.75}\text{Sm}_{1.75}\text{Cl}_6$, the $[\text{SmCl}_9]^{6-}$ tricapped trigonal prisms form a 1D structural backbone, creating 1D channels along the c axis for fast Na^+ -ion diffusion (Figure 8b). Due to the polycrystalline microstructure, long-range Na^+ -ion diffusion is hindered by the grain boundaries. Apparently, the high-coordination UCl_3 -type lattice induces the amorphization of surrounding low-coordination halides ($\text{C.N.} \leq 6$), such as NaTaCl_6 , characterized by disordered $[\text{TaCl}_6]^-$ octahedra. The resulting heterogeneous framework of crystalline and amorphous regions is reported to facilitate fast Na^+ -ion percolation. As a result, the optimized combination of $\text{Na}_{0.75}\text{Sm}_{1.75}\text{Cl}_6:\text{NaTaCl}_6$ (composition ratio of 0.62:0.38) exhibits an ionic conductivity up to $\sigma(\text{Na}^+) = 2.7 \cdot 10^{-3} \text{ S cm}^{-1}$ at 25°C . The electrochemical stability window of the $\text{Na}_{0.75}\text{Sm}_{1.75}\text{Cl}_6$ was calculated to be [0.64, 4.25] V vs. Na^+/Na by the grand potential phase diagram approach, while the NaTaCl_6 component shows a higher reduction limit of 2.15 V vs. Na^+/Na , attributed to the reduction of Ta^{5+} . On the other hand, the amorphous nature of NaTaCl_6 contributes to the favorable deformability of the heterogeneous material as a SE. By simple cold-pressing, the SSSB using $\text{Na}_{0.85}\text{Mn}_{0.5}\text{Ni}_{0.4}\text{Fe}_{0.1}\text{O}_2$ (NMNFO) as cathode active material delivers an initial discharge capacity of $117.9 \text{ mAh g}_{\text{NMNFO}}^{-1}$ at 0.1C. With good cathode/catholyte interfacial stability, as suggested by *ex situ* XP spectra, the capacity retention after 100 cycles (at 0.2C) reaches 91%. As another example of this heterogeneous framework concept, $0.57\text{Na}_{0.75}\text{La}_{1.75}\text{Cl}_6:0.43\text{NaTaCl}_6$ exhibits a comparable ionic conductivity of $\sigma(\text{Na}^+) = 1.8 \cdot 10^{-3} \text{ S cm}^{-1}$. The schematic diagram of the proposed synergistic effect of the heterogeneous microstructure in Figure 8b shows Na^+ -ion diffusion in the crystalline bulk, the amorphous matrix and the interface.

In another study, by creating configurational disorder through mixing multiple elements on the cation site, superionic conductivity was achieved for Li^+ , Cu^+ and Ag^+ ions, whereas a lower sodium ion conductivity of $\sigma(\text{Na}^+) = 0.88 \cdot 10^{-3} \text{ S cm}^{-1}$ was exhibited by $1.5\text{NaCl}-(\text{LaCl}_3 \cdot \text{CeCl}_3 \cdot \text{ZrCl}_4 \cdot \text{HfCl}_4 \cdot \text{TaCl}_5)_{0.2}$.^[73]

4. Theoretical Investigation of Sodium Halides

Despite the successful application of several Na halides in SSSBs, the understanding of Na^+ transport properties and mechanism lags their lithium counterparts. Moreover, although high conductivities have been achieved with highly disordered amorphous materials, a breakthrough of RT Na^+ ion conductivity above 1 mS cm^{-1} is still required for crystalline halide SEs to be competitive in the solid state battery space. Given this, theoretical investigations of conductivity mechanisms in Na halides are of great significance in building the knowledge database. In recent years, first-principles calculations have been employed to screen and design possible candidates, which will be discussed in this section.

4.1. Na_3YX_6 ($\text{X} = \text{Cl}, \text{Br}$)

In 2020, Jena et al. investigated the properties of sodium-yttrium halides (Na_3YCl_6 and Na_3YBr_6) computationally, including the ionic diffusivity and electrochemical stability window as well as compatibility with electrode materials.^[74] Unlike the experimental work on Na_3YCl_6 that reports the $R\bar{3}$ space group for this phase, the ground-state structure of Na_3YCl_6 in the theoretical study is found in the space group $P321$, and consists of two parallel sets of YCl_6 octahedra that are arranged along different orientations. Na_3YBr_6 , on the other hand, adopts a $C2$ monoclinic structure. In both cases, Na and Y atoms are octahedrally coordinated with the halogens. Cation vacancies exist in the lattice near the Y site, which potentially act as sites for Na^+ ion migration to smooth the energy landscape.

The stability of the two structures was evaluated. According to the ternary phase diagrams, Na_3YBr_6 resides on the convex hull, while the E_{hull} of Na_3YCl_6 is $8.6 \text{ meV atom}^{-1}$, small enough to be compensated by the thermal energy fluctuation at RT. This suggests they have similar thermal stability. No soft phonon modes were observed over the entire Brillouin zone in the phonon spectra, suggesting dynamic stability of both materials. Computational simulations yielded activation energies for sodium ion transport in Na_3YCl_6 and Na_3YBr_6 of 0.30 and 0.32 eV, and RT Na^+ ionic conductivities of $\sigma(\text{Na}^+) = 0.77 \text{ mS cm}^{-1}$ and $\sigma(\text{Na}^+) = 0.44 \text{ mS cm}^{-1}$ were computed, respectively. The difference results from the available diffusion paths. In Na_3YCl_6 , NaCl_6 octahedra face-share along the c direction, forming channels through which Na^+ ions can hop along one dimension. In the a and b directions, NaCl_6 octahedra are edge-shared and therefore Na^+ ions move through the adjoining empty tetrahedral site to hop between two octahedral sites. Since the repulsion from adjacent YCl_6 octahedra can block this pathway, Na diffusion along the ab plane is more

restricted. In contrast, in Na_3YBr_6 , NaBr_6 octahedra share edges in all three dimensions, leading to an isotropic Na^+ diffusion network formed by *oct-tet-oct* pathways. Compared to the reported ionic conductivity value of Na_3YCl_6 ,^[37] the calculated value is 4 orders of magnitude higher which casts doubt on the assumptions of the computations [experimental result: $\sigma(\text{Na}^+) = 9.5 \cdot 10^{-8} \text{ S cm}^{-1}$,^[37] theoretical calculation: $\sigma(\text{Na}^+) = 0.77 \text{ mS cm}^{-1}$].

Apart from the good theoretical ionic conductivity, the electrochemical stability ranges of Na_3YCl_6 and Na_3YBr_6 are predicted to be fairly wide ([0.51, 3.75] V and [0.57, 3.36] V vs. Na^+/Na), extending the choice of cathode active materials. The interface chemical stability of the two SE materials with high-voltage cathodes have been evaluated. The calculated reaction energies with layered oxide cathodes (NaCoO_2 and NaCrO_2) are much smaller compared to the sulfide SE materials. Moreover, the compatibility with polyanionic cathodes ($\text{Na}_2\text{FePO}_4\text{F}$, $\text{Na}_3\text{V}_2(\text{PO}_4)_3$ and $\text{Na}_3\text{V}_2(\text{PO}_4)_2\text{F}_3$) is superior as well, suggesting potential for the application of halide-based SE materials in SSSBs.

4.2. Na_3MCl_6

To broaden the potential choices of sodium chloride SEs, Yu et al. carried out a systematic assessment on a series of Na_3MCl_6 materials with 26 M^{3+} ions.^[75] The phase stability, electrochemical stability and Na^+ ion transport properties were investigated via theoretical calculations. The crystal structures of all Na_3MCl_6 materials are comprised of NaCl_6 and MCl_6 polyhedra. Depending on the ionic radius of the M^{3+} ion, the structures mostly fall into the trigonal $P\bar{3}1c$, monoclinic $P2_1/n$ and trigonal $R\bar{3}$ space groups. By comparing the total energy differences between the phases, the most stable structure of the Na_3MCl_6 materials was found to obey the following rules: when the M^{3+} cation is relatively large (> 90 pm, including Y, Bi, Er, Ho, Dy, Tb, Gd, Eu, Sm, Pm, Nd, Pr, Ce and La), the structure prefers the trigonal $R\bar{3}$ space group; when the M^{3+} cation has an intermediate ionic radius (including V, Fe, Ti, Sc, Lu, Yb and Tm), the structure prefers a monoclinic $P2_1/n$ space group; and when the M^{3+} cation is one of the group 13 elements (Al, Ga, In, Tl) or is relatively small (Cr), the lattice adopts trigonal $P\bar{3}1c$ symmetry. Regarding phase stability, the E_{hull} of Na_3MCl_6 ($\text{M} = \text{Sc}, \text{Lu}, \text{Y}, \text{In}, \text{Tl}, \text{Bi}, \text{Yb}, \text{Tm}, \text{Er}$) exhibit negative values, suggesting stability against their decomposition products. Among them, the M^{3+} with group 3 elements and lanthanides demonstrate superior electrochemical stability, with an electrochemical stability window between 0.5 and 3.8 V vs. Na^+/Na ; while the M^{3+} with *p*-block elements show a reduction potential above 1.5 V, indicating their instability with sodium metal anodes.

The bond-valence site energy (BVSE) method was applied to predict the ion migration pathways. The ion transport properties of three different representative structures were studied: Na_3CrCl_6 (trigonal $P\bar{3}1c$, Figure 9a), Na_3ErCl_6 (monoclinic $P2_1/n$, Figure 9b) and Na_3GdCl_6 (trigonal $R\bar{3}$, Figure 9c). In trigonal structures, Na^+ ions diffuse along the z-axis through *oct-oct*

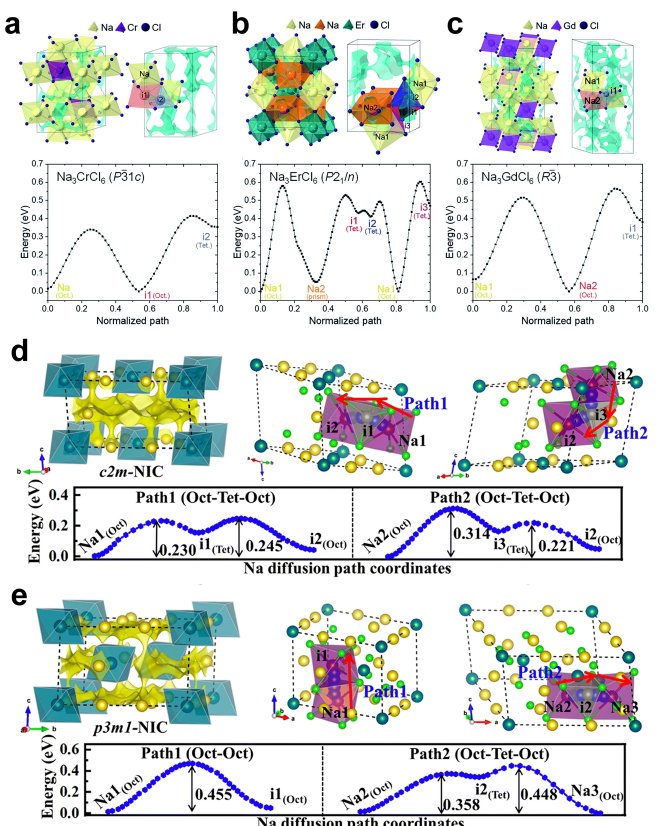


Figure 9. Na -ion migration pathways in different materials and structures predicted by the BVSE method: (a) Na_3CrCl_6 (trigonal $P\bar{3}1c$); (b) Na_3ErCl_6 (monoclinic $P2_1/n$); (c) Na_3GdCl_6 (trigonal $R\bar{3}$); (d) Na_3InCl_6 (monoclinic $C2/m$) and (e) Na_3InCl_6 (trigonal $P\bar{3}m1$). Reproduced with permission.^[75,76] Copyright © 2021 and 2023, Royal Society of Chemistry.

pathways, and through *oct-tet-oct* pathways in three dimensions. In the monoclinic structure, Na^+ ions migrate through *oct-prism* or *oct-tet-prism* pathways. The calculated activation energies in the trigonal $P\bar{3}1c$ structure are 0.34 and 0.41 eV for *oct-oct* and *oct-tet-oct* pathways, respectively, which are lower than that of the monoclinic $P2_1/n$ and trigonal $R\bar{3}$ phases. The simulated RT ionic conductivity of trigonal Na_3CrCl_6 is $\sigma(\text{Na}^+) = 2 \cdot 10^{-7} \text{ S cm}^{-1}$, significantly higher than of monoclinic Na_3ErCl_6 ($\sigma(\text{Na}^+) = 3 \cdot 10^{-10} \text{ S cm}^{-1}$), again highlighting the strong dependence of ion transport on the crystal structure. To evaluate the effect of aliovalent atom doping on M^{3+} sites, the Na^+ ion transport properties of $\text{Na}_{2.5}\text{Cr}_{0.5}\text{Zr}_{0.5}\text{Cl}_6$, $\text{Na}_{2.5}\text{Cr}_{0.5}\text{Zr}_{0.5}\text{Cl}_6$ and $\text{Na}_{2.5}\text{Cr}_{0.5}\text{Zr}_{0.5}\text{Cl}_6$ were calculated. After introducing vacancies by Zr^{4+} doping, the predicted ionic conductivities demonstrate up to four orders of magnitude enhancement ($\sigma(\text{Na}^+) \sim 10^{-5} \text{ S cm}^{-1}$). The size difference between M and Zr octahedra also induces disorder, which contributes to the increase in Na^+ ion mobility.

Ouyang et al. also carried out a detailed study on the structure-property correlations of Na_3InCl_6 and Na_3ScCl_6 materials.^[76] Apart from the above-mentioned $P\bar{3}1c$ Na_3InCl_6 and $P2_1/n$ Na_3ScCl_6 , they also reported promising stability of the monoclinic $C2/m$ and trigonal $P\bar{3}m1$ polymorphs of both materials, which are theoretically synthesizable. The electrochemical stability windows of $C2/m$ - Na_3InCl_6 and $P\bar{3}m1$ - Na_3InCl_6

are 2.18–4.04 V and 2.45–3.89 V, respectively, while the windows of $C2/m$ - Na_3ScCl_6 and $P\bar{3}m1$ - Na_3ScCl_6 are 0.83–3.79 V and 1.01–3.66 V, respectively. The inferior reduction stability of Na_3InCl_6 is also observed in its $P\bar{3}1c$ structure polymorph (2.15 V). Both of the halides also exhibit good compatibility with polyanionic cathodes (NaFePO_4 and $\text{Na}_3\text{V}_2(\text{PO}_4)_3$), outperforming the sulfide SEs.

Apart from ionic conductivity, another important requirement for SE materials is to exhibit good mechanical properties that allow cold pressing. Hence, the elastic properties of Na_3InCl_6 and Na_3ScCl_6 were also evaluated by calculating the elastic constants; several elastic moduli are presented, including bulk modulus (B), shear modulus (G) and Young's modulus (E). The size of the calculated moduli follows the trend of $P\bar{3}m1 > P\bar{3}1c (P2_1/n) > C2/m$, and the values of Na_3ScCl_6 are larger than those of Na_3InCl_6 , suggesting higher hardness and stiffness. This could be attributed to the stronger Sc–Cl bonds compared to the In–Cl bonds resulting from the lower electronegativity of Sc, and thus better elastic properties of Na_3ScCl_6 among the studied materials. It is worthy to note that all of the polymorphs of Na_3InCl_6 and Na_3ScCl_6 , except for the $C2/m$ phases, exhibit Pugh's ratios (B/G) higher than 1.75. This is higher than of the analogous lithium metal chlorides, indicating better ductility of the Na compounds. The overall elastic moduli are also comparable to sodium sulfide (Na_3PS_4),^[77] suggesting good mechanical properties.

Na^+ ion migration was compared in detail for the In and Sc halides. In $P\bar{3}1c$ - Na_3InCl_6 and $P2_1/n$ - Na_3ScCl_6 , a high migration barrier and low ionic conductivity were observed, consistent with the previous results. In contrast, the $P\bar{3}m1$ and $C2/m$ polymorphs exhibit a sublattice with almost 25% Na vacancies, which may aid Na migration. For the $C2/m$ structure (Figure 9d), both materials exhibit two-dimensional oct-tet-oct pathways, whereas for the $P\bar{3}m1$ structure (Figure 9e), both materials exhibit 3D diffusion channels through direct oct-oct or oct-tet-oct pathways. The simulated Arrhenius plots of the $P\bar{3}m1$ and $C2/m$ structured halides suggest high RT ionic conductivities in the range of 0.66–11.54 mS cm⁻¹, and low activation energies in the range of 0.20–0.33 eV, which so far have not been proven experimentally.

4.3. Na_3MBr_6

Compared to chlorides, bromides with larger lattice frameworks can widen the bottleneck for cation migration, and thus provide higher ionic conductivity. Zhang et al. studied a series of sodium bromides (Na_3MBr_6) to evaluate their possible application as SEs.^[78] Similar to the Na_3MCl_6 phases studied by Yu et al.,^[75] the thermodynamically preferred crystal structure of Na_3MBr_6 also depends on the type and ionic radius of M^{3+} . When the ion radius of M^{3+} is small (V, Sc, Lu) or for group 13 and group 15 elements (In, Tl, Bi), Na_3MBr_6 tends to crystallize in trigonal $P\bar{3}1c$ phases; when the ion radius of M^{3+} is large (Eu, Sm, Pm, Nd, Pr, Ce, La), trigonal $R\bar{3}$ structures tend to be formed; while for M^{3+} with intermediate ion radii, monoclinic $P2_1/n$ structures are found. Based on that, three representatives

were investigated in detail: $P\bar{3}1c$ - Na_3ScBr_6 , $P2_1/n$ - Na_3YBr_6 and $R\bar{3}$ - Na_3SmBr_6 . The Na^+ ion diffusion pathways were assessed by the BVSE method. In the monoclinic $P2_1/n$ phase, sodium cations on two different sites form either octahedral or prismatic coordination with Br anions. The diffusion pathways are three-dimensional. Between octahedral and prismatic sites, Na^+ ions hop along *oct-tet-tet-prism* pathways, while between prismatic and octahedral sites, Na^+ ions hop along *prism-tet-oct* pathways. In trigonal phases, Na^+ ions migrate along the z axis through *oct-oct* sites or through *oct-tet-oct* pathways in three dimensions, which is similar to Na_3CrCl_6 and Na_3GdCl_6 .^[75] Activation energies of all diffusion pathways show the lowest migration barrier of 0.39 eV in $P\bar{3}1c$ - Na_3ScBr_6 , indicative of better ionic diffusivity than in the $P2_1/n$ - and $R\bar{3}$ -polymorphs.

Band gaps ΔE_g of the Na_3MBr_6 compounds were calculated to estimate the electronic conductivity. The values fall between 3.28 to 5.16 eV, suggesting a relatively low electronic partial conductivity. Especially, Na_3MBr_6 phases with $M = d$ - and f -block elements exhibit a wider band gap compared with p -block elements, leading to lower electronic conductivity, and thus, also to a wider electrochemical stability window. The average oxidation onset potential of Na_3MBr_6 phases is around 3.2 eV, which is 0.6 eV lower than the corresponding Na_3MCl_6 . Nevertheless, oxidation may be suppressed by kinetic barriers to decomposition in practice. Regarding cathode compatibility, Na_3MBr_6 is predicted to be stable against phosphates (NaFePO_4 and $\text{Na}_3\text{V}_2(\text{PO}_4)_3$), while decomposition reactions can easily occur between Na_3MBr_6 and layered oxides ($\text{NaNi}_{1/3}\text{Co}_{1/3}\text{Mn}_{1/3}\text{O}_2$ and NaCoO_2). Therefore, surface coatings are essential for the latter in combination with Na_3MBr_6 SEs.

4.4. Na_3MI_6

Down the periodic table, iodides with yttrium as the central metal cation have also been studied, with the purpose of understanding the structural dependence of Na^+ ion migration. Wang et al. used first-principle calculations and data-mining techniques to examine the Na^+ transport properties of Na_3YI_6 in three polymorphs with space groups of $C2/m$, $P\bar{3}m1$, $P\bar{3}1c$.^[79] The iodine sublattice exhibits a face-centered cubic (*fcc*) arrangement in a $C2/m$ polymorph and *hcp* configuration in $P\bar{3}m1$, $P\bar{3}1c$ polymorphs, respectively. All three structures exhibit E_{hull} values above zero, indicative of their metastable nature. Nevertheless, since the E_{hull} of $C2/m$ and $P\bar{3}1c$ phases are only 7.00 and 8.82 meV atom⁻¹, the syntheses of these phases may be possible considering the entropic contribution. The indirect bandgaps are larger than 3.2 eV, suggesting a modestly wide electrochemical stability window.

The predicted ionic conductivities of the $C2/m$ - Na_3YI_6 and $P\bar{3}m1$ - Na_3YI_6 phases are $\sigma(\text{Na}^+) = 0.35$ and 0.18 mS cm⁻¹, with activation energies of 316 and 351 meV, respectively, comparable to those of Na_3YCl_6 and Na_3YBr_6 . Nevertheless, the $P\bar{3}1c$ structured phase shows poor Na^+ ion conductivity of only $9.1 \cdot 10^{-6}$ S cm⁻¹, with an activation energy of 454 meV (Figure 10a). This largely results from the ion diffusion pathway.

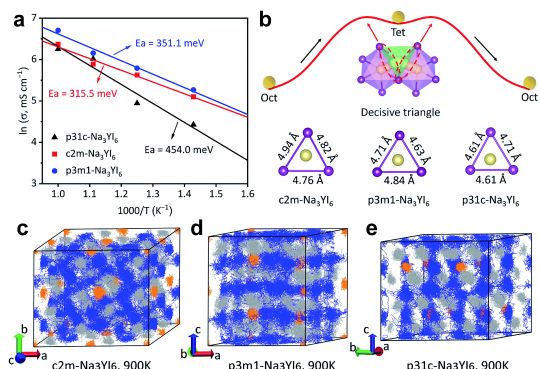


Figure 10. Predicted Na-ion migration in different Na_3YI_6 polymorphs: (a) Arrhenius plot of the Na ionic conductivity versus $1/T$; (b) schematic of Na ion diffusion from one equilibrium site to the next along the *oct-tet-oct* pathway. The maximum migration energy is determined by the difficulty of Na ion transport through the triangular face; (c) the ionic trajectories of three polymorphs from the AIMD simulations at 900 K. Reproduced with permission.^[79] Copyright © 2021, Royal Society of Chemistry.

According to AIMD simulations, Na^+ ion diffusion in both the $C2/m$ and $P\bar{3}m1$ phases follows 3D cross-linked networks, while the pathway in the $P\bar{3}1c$ structure proceeds along 1D channels (Figure 10c–e). Moreover, the adjacent YI_6 octahedra along the c -axis block ion diffusion, which contributes to the limited ionic conductivity in this polymorph. The corresponding energy barriers of different pathways were also calculated by the climbing image nudged elastic band (CI-NEB) method. In $C2/m\text{-Na}_3\text{YI}_6$, Na ions diffuse through a three-dimensional cross-linked network in the *fcc* lattice along *oct-tet-oct* pathways, with migration barriers of 0.339 eV. In $P\bar{3}m1\text{-Na}_3\text{YI}_6$, a cross-linked network in the *hcp* sublattice is also observed, where Na^+ ions hop along either direct *oct-oct* pathways or *oct-tet-oct* pathways. The energy barriers in the two types of pathways are similar, 0.384 and 0.354 eV, respectively. In sharp contrast, the *oct-oct* diffusion pathway in the $P\bar{3}1c\text{-Na}_3\text{YI}_6$ sublattice is blocked by the YI_6 octahedra, corroborating the AIMD results. The energy barrier for direct migration along the *oct-oct* pathway is only 0.22 eV, however, a migration barrier of 0.42 eV is needed to overcome blocking of the YI_6 octahedra.

Using data mining techniques, the diffusion dynamics at 700 K and 900 K were visualized in distribution hot maps. At higher temperatures, the *oct-tet-oct* pathways in $P\bar{3}1c\text{-Na}_3\text{YI}_6$ also become available for effective Na^+ ion diffusion. Based on the above investigations, it was concluded that the *oct-tet-oct* pathway dominates Na^+ ion conduction in Na_3YI_6 polymorphs, and the limiting migration energy for Na diffusion through adjacent *oct* sites is determined by diffusion through the triangular face (Figure 10b). The $P\bar{3}m1$ phase shows the smallest area, which explains the poor ionic conductivity and high migration barrier.

Based on the above study, the same group also carried out systematic investigations on different sodium iodide superionic conductors Na_3MI_6 ($M = \text{Sc}, \text{Y}, \text{La}, \text{In}$) with a monoclinic $C2/m$ structure.^[80] Compared with other possible space groups, $C2/m\text{-Na}_3\text{MI}_6$ exhibits the lowest E_{hull} value, indicating better thermodynamic stability. In addition, the Na vacancies (1/3) on the

octahedral sites are beneficial for Na^+ ion transport. However, the E_{hull} of Na_3InI_6 reaches 52.3 meV atom $^{-1}$, much higher than the RT thermal energy $k_B T$ of ~ 26 meV atom $^{-1}$, which makes its synthesis unlikely. The RT ionic conductivities of Na_3ScI_6 , Na_3YI_6 , and Na_3LaI_6 were simulated by AIMD, yielding values of 0.36, 0.35, 0.20 mS cm $^{-1}$, respectively, with activation energies between 0.32 and 0.37 eV. Encouragingly, the conductivities are comparable to sulfide SEs such as $\text{Na}_{10}\text{SnP}_2\text{S}_{12}$ (0.4 mS cm $^{-1}$) and $\text{Na}_{11}\text{Sn}_2\text{PS}_{12}$ (1.4 mS cm $^{-1}$),^[7,17] suggesting they can be potential candidates for sodium SEs. Experimental works are waiting to be carried out to validate the superior RT ionic conductivities. Similar to the previous study, Na^+ ions also diffuse along two types of pathways: along *oct-tet-oct* pathways or directly hop between two *oct* sites although the latter requires overcoming a larger activation energy. Furthermore, the relatively lower phonon band centers of the partially occupied Na sites suggest the preference of Na^+ transport inside the layers where Na sites are only partially occupied, again indicating the significant role of vacancies in the $C2/m$ structure. However, as expect the electrochemical stability window of the iodides is narrower compared to chlorides and bromides, with an oxidation onset voltage of only 2.6 V. Moreover, the decomposition energies of interfaces between Na_3MI_6 and different cathode materials (layered oxide and polyanionic cathodes) are also smaller. The tradeoff between ionic conductivity and electrochemical stability needs to be considered when developing halide materials for Na SEs.

4.5. Na_3MX_6

Chung et al. carried out a comprehensive investigation on a wide range of sodium halides, Na_3MX_6 (where $X = \text{Cl}, \text{Br}, \text{I}$) to unravel the factors governing the crystal structure.^[81] Generally, chlorides and bromides tend to form trigonal $P\bar{3}1c$, monoclinic $P2_1/n$ and trigonal $R\bar{3}$ phases, where their relative stability is determined by the ionic radius of the M^{3+} ions. For iodides, the monoclinic $C2/m$ space group is preferred (Figure 11a). In addition, the increase in ion radius of the halogen X^- decreases the phase stability. The observation agrees well with the previous results. The phase preference of Na_3MX_6 can be defined by the octahedral factor (t) between M and X – $t_{\text{MX}}(r_{\text{M}}/r_X)$ – while the octahedral factor between A (Li, Na) and X is termed as $t_{\text{AX}}(r_A/r_X)$ to compare the sodium and lithium systems. The $t_{\text{MX}}-t_{\text{AX}}$ plot presents the phase preference and phase transitions as a function of ion radii (Figure 11b) where the dashed line represents cases where the MX_6 and AX_6 octahedra have comparable sizes. Na_3MX_6 ($X = \text{Cl}, \text{Br}, \text{I}$) and Li_3MX_6 ($X = \text{Cl}, \text{Br}$) are positioned below and above the dashed line, respectively, due to the larger and smaller ion radius of Na^+ and Li^+ . Na_3MI_6 exhibits a similar octahedral factor compared to Li_3MCl_6 , and as a result both of them prefer the monoclinic $C2/m$ structure. With relatively small M^{3+} ions such as Al and Ga, NaMX_4 ($P2_12_12_1$) is formed instead of Na_3MX_6 . The phase transition trend shows different behavior for *p*-block elements and *d*-/*f*-block elements, which is attributed to the difference in the electronegativity between M and X (Figure 11c–d).

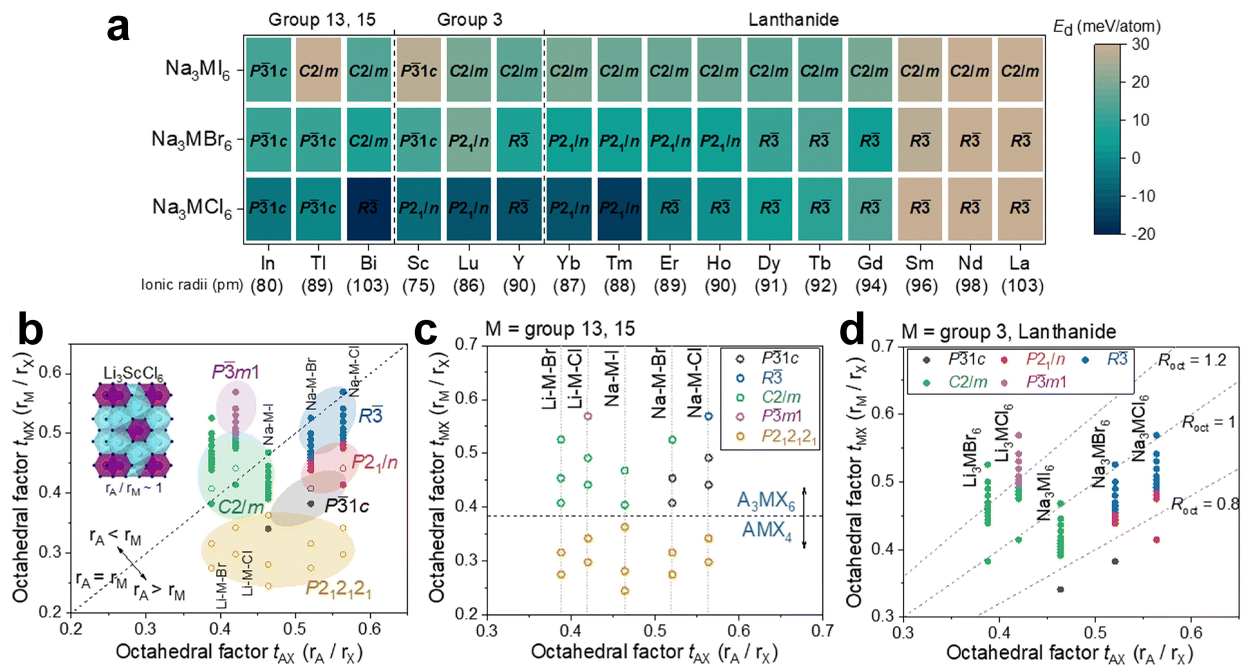


Figure 11. Predicted preferred crystal structure of sodium halides: (a) heat map of decomposition energy; (b-d) preferred structure as a function of octahedral factors. Reproduced with permission.^[81] Copyright © 2022, Royal Society of Chemistry.

In general, high ionic conductivities can be observed in monoclinic $C2/m$ phases due to the 3D diffusion pathways, consistent with previous studies. Moreover, Br–I ion mixing on the halogen site can further enhance the ionic conductivity owing to disorder. $\text{Na}_3\text{GdBr}_3\text{I}_3$ is predicted to exhibit a Na^+ ion conductivity of 7.5 mS cm^{-1} , which is the highest value predicted among the reported Na halides although it is not expected to exhibit high anodic stability. The results in this study provide principal design guidelines for the development of halide-based Na SEs. As before, there is no experimental proof yet available.

4.6. Halides with Spinel-Type Structure

Apart from the materials discussed above, several chlorides with a spinel structure have also been explored computationally. Sun et al. reported a new spinel-type chloride, $\text{Na}_2\text{Y}_{2/3}\text{Cl}_4$, as a superionic sodium-ion conductor.^[82] The spinel skeleton is formed by edge-sharing MCl_6 ($\text{M}=\text{Na}, \text{Y}$ in $16d$ site) octahedra. Na ions partially occupy the $8a$ (tetrahedral), $16c$ (octahedral) and $48f$ (tetrahedral) sites. The tetrahedral and octahedral sites are connected by face-sharing and form three-dimensional diffusion pathways for Na^+ ions, typical of a spinel. The ground state of $\text{Na}_2\text{Y}_{2/3}\text{Cl}_4$ shows an E_{hull} value of 13 meV atom^{-1} , indicating thermodynamic stability.

The RT ionic conductivity is predicted to be 0.94 mS cm^{-1} . Activation energy values in the three directions are similar, $\sim 0.29 \text{ eV}$, indicating isotropic diffusion pathways. The migration barriers of Na ions on different Wyckoff positions were also compared. The results suggest that the Na atom on the $16d$ site tends to be immobile, while $8a$ -site Na ions can jump with a

low migration barrier of 0.13 eV (Figure 12a–d). The computed electrochemical window of $\text{Na}_2\text{Y}_{2/3}\text{Cl}_4$ spinel is 0.59 to 3.76 V , similar to that of Na_3YCl_6 , which should provide good oxidation

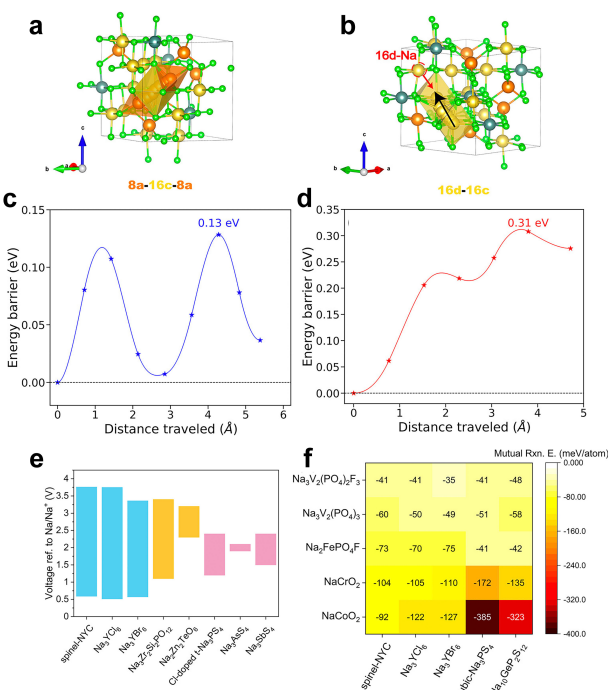


Figure 12. Predicted properties of spinel-type $\text{Na}_2\text{Y}_{2/3}\text{Cl}_4$: the migration path and corresponding energy barriers of (a, c) $8a$ -Na along the diffusion network and (b, d) $16d$ -Na migration onto an adjacent $16c$ site; (e) calculated electrochemical windows compared with other sodium SEs. (f) heat map of calculated mutual reaction energy between solid electrolytes and cathodes.^[82] Copyright © 2023, American Chemical Society.

stability towards high-voltage cathodes (Figure 12e–f). The spinel structure can also incorporate other metal ions, such as Sc, In, Er, et al., and most of them exhibit a borderline E_{hull} value of $\sim 25 \text{ meV atom}^{-1}$. According to another case study by Xia et al.,^[83] the $\text{Na}_2\text{In}_x\text{Sc}_{0.666-x}\text{Cl}_4$ spinel exhibits a maximum ionic conductivity of 0.22 mS cm^{-1} ($x=0.666$), with an activation energy of 0.22 eV . However, the electrochemical window is much narrower ($2.15\text{--}3.76 \text{ V}$) due to the presence of the *p*-block element, In. It is hypothesized that ion substitution can further increase the conductivity of spinel SEs but this remains to be tested experimentally.

5. Conclusions and Outlook

In this review, the current progress of sodium halide-based SEs is summarized, focusing on SEs with complex MX_y polyhedra as structural key units. Although the ion-conduction properties still need to be improved compared to lithium SEs, preliminary experimental results have verified that halide materials, especially chlorides, can be good catholyte materials in cathode composites in SSSBs, showing minor interfacial side reactions but yet lacking sufficient Na^+ mobility. The impact of the synthesis procedure (such as heating parameters, cooling protocols) on the crystal structure is discussed; and structure-conductivity correlations are presented, based on which aliovalent atom doping strategies have been performed to optimize the RT ionic conductivity. In recent studies on crystalline materials, a maximum ionic conductivity of $\sigma(\text{Na}^+)=6.6 \cdot 10^{-5} \text{ Scm}^{-1}$ at RT was achieved experimentally, with a monoclinic phase ($P2_1/n$) of composition $\text{Na}_{2.125}\text{Y}_{0.125}\text{Zr}_{0.875}\text{Cl}_6$ (NYZCl). Extensive theoretical investigations were carried out to screen and design possible other candidates as SEs. These results revealed the lowest energy crystal structure, predicted ionic conductivity and sodium migration pathways, electrochemical properties and compatibility with cathode materials. Generally, iodides are predicted to show the highest ionic conductivity but narrowest electrochemical stability window – as expected. Chlorides and bromides show higher oxidation stability but their ionic conductivities are smaller. Therefore, a tradeoff is always unavoidable when designing halide SEs with high performance. Meanwhile, the discrepancy between theory and experiments is significant in some cases and calls for resolution. It will be interesting to see whether experimentalists succeed in synthesizing some of the theoretically predicted candidates – and whether the predictions of their properties then hold.

The most urgent challenges of development of halide SEs for SSBs can be summarized as follows. *First of all*, the RT ionic conductivity needs to be improved. While a reasonable separator electrolyte requires not more than 0.1 mS cm^{-1} , which is almost met by NYZCl, a good catholyte should ideally show a conductivity of up to 10 mS cm^{-1} to allow operation competitive with liquid systems. Several theoretical studies also point out differences in the preferred crystal structures for Na_3MX_6 vs Li_3MX_6 – mostly the result of the different ionic radius of Li^+ and Na^+ – which leads to different ion migration behavior. This

may inspire us to veer away from swapping Li^+ for Na^+ in typical Li^+ superionic halides and search for unique structures for Na^+ -ion conduction. Beyond long-range ordered materials, the exploration of amorphous SE materials suggests that the diffusion of Na^+ ions may be facilitated by the weakened interaction between charge carriers and the disordered supporting matrix through mechanochemical synthesis, pushing the ionic conductivity up to $\sigma(\text{Na}^+, \text{RT})=4 \cdot 10^{-3} \text{ Scm}^{-1}$ to date (NaTaCl_6). The role of impurities potentially introduced by long-term ball milling merits further investigation. Similarly, glassy oxychloride SEs were reported very recently ($\text{NaAlCl}_{2.5}\text{O}_{0.75}$)^[84] and $0.5\text{Na}_2\text{O}_2\text{-TaCl}_5$ ^[85] with promising conductivity. It is suggested that substituting chlorine by oxygen in the anion sublattice could also break the long-range periodic ordering, leading to fast Na^+ -ion diffusion. The idea of amorphization could pave a new way for the design of future sodium halide SEs.

Secondly, the dominating factor to facilitate Na^+ migration still needs to be well understood. Conductivity is likely limited by bottlenecks created by migration of the large Na^+ ion through trigonal halide faces in the structures under consideration. Synergistic anion sublattice dynamics, such as $\text{YCl}_6^{3-}/\text{ZrCl}_6^{2-}$ octahedral rotation in $\text{Na}_{2.125}\text{Y}_{0.125}\text{Zr}_{0.875}\text{Cl}_6$, is already known to be beneficial for Na^+ cation diffusion, and is worth further investigation.

Thirdly, the instability of these halides at low potentials, especially those with *p*-block metal elements, needs to be considered. For example, an artificial solid electrolyte interface at the negative electrode might be introduced. Addressing the above challenges can undoubtedly enable transformative advances for SSSBs.

Acknowledgements

This work was funded by the German Research Foundation (DFG) under Project ID 390874152 (POLiS Cluster of Excellence). L. F. N. acknowledges the support of NSERC through the Discovery and Canada Research Chair programs, and the Ontario Research Foundation. Open Access funding enabled and organized by Projekt DEAL.

Conflict of Interests

The authors declare no conflict of interest.

Keywords: solid electrolytes · sodium ternary halides · sodium batteries · solid state batteries · catholytes

- [1] Y. Li, F. Wu, Y. Li, M. Liu, X. Feng, Y. Bai, C. Wu, *Chem. Soc. Rev.* **2022**, *51*, 4484.
- [2] Y. Jin, P. M. L. Le, P. Gao, Y. Xu, B. Xiao, M. H. Engelhard, X. Cao, T. D. Vo, J. Hu, L. Zhong, B. E. Matthews, R. Yi, C. Wang, X. Li, J. Liu, J.-G. Zhang, *Nat. Energy* **2022**, *7*, 718.
- [3] J. Peng, W. Zhang, Q. Liu, J. Wang, S. Chou, H. Liu, S. Dou, *Adv. Mater.* **2022**, *34*, 2108384.

- [4] P. Yadav, V. Shelke, A. Patrike, M. Shelke, *Oxf. Open Mater. Sci.* **2023**, *3*, itac019.
- [5] J. Janek, W. G. Zeier, *Nat. Energy* **2023**, *8*, 230.
- [6] S. Song, H. M. Duong, A. M. Korsunsky, N. Hu, L. Lu, *Sci. Rep.* **2016**, *6*, 32330.
- [7] W. D. Richards, T. Tsujimura, L. J. Miara, Y. Wang, J. C. Kim, S. P. Ong, I. Uechi, N. Suzuki, G. Ceder, *Nat. Commun.* **2016**, *7*, 11009.
- [8] Z. Zhang, Q. Zhang, J. Shi, Y. S. Chu, X. Yu, K. Xu, M. Ge, H. Yan, W. Li, L. Gu, Y. Hu, H. Li, X. Yang, L. Chen, X. Huang, *Adv. Energy Mater.* **2017**, *7*, 1601196.
- [9] B. Tang, X. Yu, Y. Gao, S.-H. Bo, Z. Zhou, *Sci. Bull.* **2022**, *67*, 2149.
- [10] Y. Lu, L. Li, Q. Zhang, Z. Niu, J. Chen, *Joule* **2018**, *2*, 1747.
- [11] T. Famprikis, P. Canepa, J. A. Dawson, M. S. Islam, C. Masquelier, *Nat. Mater.* **2019**, *18*, 1278.
- [12] R. Collongues, D. Gourier, A. Kahn, J. P. Boilot, Ph. Colombari, A. Wicker, *J. Phys. Chem. Solids* **1984**, *45*, 981.
- [13] M. Bay, M. Wang, R. Grissa, M. V. F. Heinz, J. Sakamoto, C. Battaglia, *Adv. Energy Mater.* **2020**, *10*, 1902899.
- [14] Y. Lu, J. A. Alonso, Q. Yi, L. Lu, Z. L. Wang, C. Sun, *Adv. Energy Mater.* **2019**, *9*, 1901205.
- [15] Z. Sun, L. Li, C. Sun, Q. Ni, Y. Zhao, H. Wu, H. Jin, *Nano Lett.* **2022**, *22*, 7187.
- [16] T. Ortmann, S. Burkhardt, J. K. Eckhardt, T. Fuchs, Z. Ding, J. Sann, M. Rohnke, Q. Ma, F. Tietz, D. Fattakhova-Rohlfing, C. Kübel, O. Guillou, C. Heiliger, J. Janek, *Adv. Energy Mater.* **2023**, *13*, 2202712.
- [17] Z. Zhang, E. Ramos, F. Lalère, A. Assoud, K. Kaup, P. Hartman, L. F. Nazar, *Energy Environ. Sci.* **2018**, *11*, 87.
- [18] M. Duchardt, U. Ruschewitz, S. Adams, S. Dehnen, B. Roling, *Angew. Chem. Int. Ed.* **2018**, *57*, 1351.
- [19] Z. Zhu, I.-H. Chu, Z. Deng, S. P. Ong, *Chem. Mater.* **2015**, *27*, 8318.
- [20] T. Famprikis, O. U. Kudu, J. A. Dawson, P. Canepa, F. Fauth, E. Suard, M. Zbirli, D. Dambournet, O. J. Borkiewicz, H. Bouyanif, S. P. Emge, S. Crete, J.-N. Chotard, C. P. Grey, W. G. Zeier, M. S. Islam, C. Masquelier, *J. Am. Chem. Soc.* **2020**, *142*, 18422.
- [21] A. Banerjee, K. H. Park, J. W. Heo, Y. J. Nam, C. K. Moon, S. M. Oh, S. Hong, Y. S. Jung, *Angew. Chem.* **2016**, *128*, 9786.
- [22] A. Hayashi, N. Masuzawa, S. Yubuchi, F. Tsuji, C. Hotehama, A. Sakuda, M. Tatsumisago, *Nat. Commun.* **2019**, *10*, 5266.
- [23] O. Maus, M. T. Agne, T. Fuchs, P. S. Till, B. Wankmiller, J. M. Gerdes, R. Sharma, M. Heere, N. Jalarvo, O. Yaffe, M. R. Hansen, W. G. Zeier, *J. Am. Chem. Soc.* **2023**, *145*, 7147.
- [24] S. Wenzel, T. Leichtweiss, D. A. Weber, J. Sann, W. G. Zeier, J. Janek, *ACS Appl. Mater. Interfaces* **2016**, *8*, 28216.
- [25] E. A. Wu, C. S. Kompella, Z. Zhu, J. Z. Lee, S. C. Lee, I.-H. Chu, H. Nguyen, S. P. Ong, A. Banerjee, Y. S. Meng, *ACS Appl. Mater. Interfaces* **2018**, *10*, 10076.
- [26] X. Li, J. Liang, X. Yang, K. R. Adair, C. Wang, F. Zhao, X. Sun, *Energy Environ. Sci.* **2020**, *13*, 1429.
- [27] H. Kwak, S. Wang, J. Park, Y. Liu, K. T. Kim, Y. Choi, Y. Mo, Y. S. Jung, *ACS Energy Lett.* **2022**, *7*, 1776–1805.
- [28] S. Wang, Q. Bai, A. M. Nolan, Y. Liu, S. Gong, Q. Sun, Y. Mo, *Angew. Chem. Int. Ed.* **2019**, *58*, 8039.
- [29] C. Wang, J. Liang, J. T. Kim, X. Sun, *Sci. Adv.* **2022**, *8*, eadc9516.
- [30] T. Asano, A. Sakai, S. Ouchi, M. Sakaida, A. Miyazaki, S. Hasegawa, *Adv. Mater.* **2018**, *30*, 1803075.
- [31] S. Y. Kim, K. Kaup, C.-H. Park, A. Assoud, L. Zhou, J. Liu, X. Wu, L. F. Nazar, *ACS Materials Lett.* **2021**, *3*, 930.
- [32] H. Kwak, D. Han, J. Lyoo, J. Park, S. H. Jung, Y. Han, G. Kwon, H. Kim, S. Hong, K. Nam, Y. S. Jung, *Adv. Energy Mater.* **2021**, *11*, 2003190.
- [33] S. R. Combs, P. K. Todd, P. Gorai, A. E. Maughan, *J. Electrochem. Soc.* **2022**, *169*, 040551.
- [34] R. Schlem, S. Muy, N. Prinz, A. Banik, Y. Shao-Horn, M. Zobel, W. G. Zeier, *Adv. Energy Mater.* **2020**, *10*, 1903719.
- [35] E. Sebti, H. A. Evans, H. Chen, P. M. Richardson, K. M. White, R. Giovine, K. P. Koiralal, Y. Xu, E. Gonzalez-Correa, C. Wang, C. M. Brown, A. K. Cheetham, P. Canepa, R. J. Clément, *J. Am. Chem. Soc.* **2022**, *144*, 5795.
- [36] R. Schlem, A. Banik, M. Eckardt, M. Zobel, W. G. Zeier, *ACS Appl. Energ. Mater.* **2020**, *3*, 10164.
- [37] E. A. Wu, S. Banerjee, H. Tang, P. M. Richardson, J.-M. Doux, J. Qi, Z. Zhu, A. Grenier, Y. Li, E. Zhao, G. Deysher, E. Sebti, H. Nguyen, R. Stephens, G. Verbist, K. W. Chapman, R. J. Clément, A. Banerjee, Y. S. Meng, S. P. Ong, *Nat. Commun.* **2021**, *12*, 1256.
- [38] E. Sebti, J. Qi, P. M. Richardson, P. Ridley, E. A. Wu, S. Banerjee, R. Giovine, A. Cronk, S.-Y. Ham, Y. S. Meng, S. P. Ong, R. J. Clément, *J. Mater. Chem. A* **2022**, *10*, 21565.
- [39] T. Zhao, A. N. Sobolev, R. Schlem, B. Helm, M. A. Kraft, W. G. Zeier, *ACS Appl. Energ. Mater.* **2023**, *6*, 4334–4341.
- [40] H. Kwak, J. Lyoo, J. Park, Y. Han, R. Asakura, A. Remhof, C. Battaglia, H. Kim, S.-T. Hong, Y. S. Jung, *Energy Storage Mater.* **2021**, *37*, 47.
- [41] J. Park, J. P. Son, W. Ko, J.-S. Kim, Y. Choi, H. Kim, H. Kwak, D.-H. Seo, J. Kim, Y. S. Jung, *ACS Energy Lett.* **2022**, *7*, 3293.
- [42] Y. Hu, J. Fu, J. Xu, J. Luo, F. Zhao, H. Su, Y. Liu, X. Lin, W. Li, J. T. Kim, X. Hao, X. Yao, Y. Sun, J. Ma, H. Ren, M. Yang, Y. Huang, X. Sun, *Matter.* **2024**, *7*, 1018–1034.
- [43] Y. Fouque, M. Gaune-Escard, W. Szczepaniak, A. Bogacz, *J. Chim. Phys.* **1978**, *75*, 360.
- [44] A. Bogacz, J. Bros, M. Gaune-Escard, A. W. Hewat, J. C. Taylor, *J. Phys. C* **1980**, *13*, 5273.
- [45] A. W. Hewat, J. C. Taylor, M. Gaune-Escard, J. P. Bros, W. Szczepaniak, A. Bogacz, *J. Phys. C* **1984**, *17*, 4587.
- [46] F. Lissner, K. Krämer, T. Schleid, G. Meyer, Z. Hu, G. Kaindl, *Z. Anorg. Allg. Chem.* **1994**, *620*, 444.
- [47] M. S. Wickleder, G. Meyer, *Z. Anorg. Allg. Chem.* **1998**, *624*, 1577.
- [48] H. D. Lutz, K. Wusow, P. Kuske, *Z. Naturforsch. B* **1987**, *42*, 1379.
- [49] R. Kanno, Y. Takeda, K. Murata, O. Yamamoto, *Solid State Ionics* **1990**, *39*, 233.
- [50] F. Stenzel, G. Meyer, *Z. Anorg. Allg. Chem.* **1993**, *619*, 652.
- [51] H.-J. Steiner, H. D. Lutz, *Z. Anorg. Allg. Chem.* **1992**, *613*, 26.
- [52] K. Yamada, K. Kumano, T. Okuda, *Solid State Ionics* **2005**, *176*, 823.
- [53] M. O'keeffe, J.-O. Bovin, *Science* **1979**, *206*, 599.
- [54] Y. Zhao, L. L. Daemen, *J. Am. Chem. Soc.* **2012**, *134*, 15042.
- [55] W. Xia, Y. Zhao, F. Zhao, K. Adair, R. Zhao, S. Li, R. Zou, Y. Zhao, X. Sun, *Chem. Rev.* **2022**, *122*, 3763.
- [56] W. Feng, L. Zhu, X. Dong, Y. Wang, Y. Xia, F. Wang, *Adv. Mater.* **2023**, *35*, e2210365.
- [57] E. Ahiavi, J. A. Dawson, U. Kudu, M. County, M. S. Islam, O. Clemens, C. Masquelier, T. Famprikis, *J. Power Sources* **2020**, *471*, 228489.
- [58] Y. Wang, Q. Wang, Z. Liu, Z. Zhou, S. Li, J. Zhu, R. Zou, Y. Wang, J. Lin, Y. Zhao, *J. Power Sources* **2015**, *293*, 735.
- [59] H. Nguyen, S. Hy, E. Wu, Z. Deng, M. Samiee, T. Yersak, J. Luo, S. P. Ong, Y. S. Meng, *J. Electrochem. Soc.* **2016**, *163*, A2165.
- [60] J. Zhu, Y. Wang, S. Li, J. W. Howard, J. Neuefeind, Y. Ren, H. Wang, C. Liang, W. Yang, R. Zou, C. Jin, Y. Zhao, *Inorg. Chem.* **2016**, *55*, 5993.
- [61] T. H. Wan, Z. Lu, F. Ciucci, *J. Power Sources* **2018**, *390*, 61.
- [62] H. Fang, P. Jena, *ACS Appl. Mater. Interfaces* **2019**, *11*, 963.
- [63] Y. Yu, Z. Wang, G. Shao, *J. Mater. Chem. A* **2018**, *6*, 19843.
- [64] J. A. Dawson, H. Chen, M. S. Islam, *J. Phys. Chem. C* **2018**, *122*, 23978.
- [65] Z. Liu, S. Ma, J. Liu, S. Xiong, Y. Ma, H. Chen, *ACS Energy Lett.* **2021**, *6*, 298.
- [66] H. Kwak, J.-S. Kim, D. Han, J. S. Kim, J. Park, G. Kwon, S.-M. Bak, U. Heo, C. Park, H.-W. Lee, K.-W. Nam, D.-H. Seo, Y. S. Jung, *Nat. Commun.* **2023**, *14*, 2459.
- [67] R. Schlem, T. Bernges, C. Li, M. A. Kraft, N. Minafra, W. G. Zeier, *ACS Appl. Energ. Mater.* **2020**, *3*, 3684.
- [68] X. Li, J. Liang, J. Luo, M. N. Banis, C. Wang, W. Li, S. Deng, C. Yu, F. Zhao, Y. Hu, T.-K. Sham, L. Zhang, S. Zhao, S. Lu, H. Huang, R. Li, K. R. Adair, X. Sun, *Energy Environ. Sci.* **2019**, *12*, 2665.
- [69] X. Zhan, J. F. Bonnett, M. H. Engelhard, D. M. Reed, V. L. Sprenkle, G. Li, *Adv. Energy Mater.* **2020**, *10*, 2001378.
- [70] M. A. Hannan, M. M. Hoque, A. Mohamed, A. Ayob, *Renewable Sustainable Energy Rev.* **2017**, *69*, 771.
- [71] K. Motohashi, H. Tsukasaki, A. Sakuda, S. Mori, A. Hayashi, *ACS Materials Lett.* **2024**, *6*, 1178.
- [72] J. Fu, S. Wang, D. Wu, J. Luo, C. Wang, J. Liang, X. Lin, Y. Hu, S. Zhang, F. Zhao, W. Li, M. Li, H. Duan, Y. Zhao, M. Gu, T.-K. Sham, Y. Mo, X. Sun, *Adv. Mater.* **2024**, *36*, 2308012.
- [73] X. Li, Y. Xu, C. Zhao, D. Wu, L. Wang, M. Zheng, X. Han, S. Zhang, J. Yue, B. Xiao, W. Xiao, L. Wang, T. Mei, M. Gu, J. Liang, X. Sun, *Angew. Chem. Int. Ed.* **2023**, *62*, e202306433.
- [74] Y. Qie, S. Wang, S. Fu, H. Xie, Q. Sun, P. Jena, *J. Phys. Chem. Lett.* **2020**, *11*, 3376.
- [75] D. Park, K. Kim, G. H. Chun, B. C. Wood, J. H. Shim, S. Yu, *J. Mater. Chem. A* **2021**, *9*, 23037.
- [76] Y. Lian, M. Wu, B. Xu, B. He, G. Liu, J. Shi, Q. Kuang, H. Wang, C. Ouyang, *J. Mater. Chem. A* **2023**, *11*, 1906.
- [77] W. Liu, H. Sun, Y. Niu, *J. Electrochem. Soc.* **2019**, *166*, A3011.
- [78] R. Li, K. Xu, K. Liu, R. Si, Z. Zhang, *Chem. Mater.* **2022**, *34*, 8356.
- [79] H. Huang, H.-H. Wu, C. Chi, Y. Yang, J. Zheng, B. Huang, S. Wang, *J. Mater. Chem. A* **2021**, *9*, 26256.

- [80] H. Huang, C. Chi, J. Zhang, X. Zheng, Y. Wu, J. Shen, X. Wang, S. Wang, *ACS Appl. Mater. Interfaces* **2022**, *14*, 36864.
- [81] S. Yu, K. Kim, B. C. Wood, H.-G. Jung, K. Y. Chung, *J. Mater. Chem. A* **2022**, *10*, 24301.
- [82] J. Liu, S. Wang, Y. Kawazoe, Q. Sun, *ACS Materials Lett.* **2023**, *5*, 1009.
- [83] F. Hussain, P. Yu, J. Zhu, H. Xia, Y. Zhao, W. Xia, *Adv. Theory Simul.* **2023**, *6*, 2200569.
- [84] T. Dai, S. Wu, Y. Lu, Y. Yang, Y. Liu, C. Chang, X. Rong, R. Xiao, J. Zhao, Y. Liu, W. Wang, L. Chen, Y.-S. Hu, *Nat. Energy* **2023**, *8*, 1221.
- [85] X. Lin, Y. Zhao, C. Wang, J. Luo, J. Fu, B. Xiao, Y. Gao, W. Li, S. Zhang, J. Xu, F. Yang, X. Hao, H. Duan, Y. Sun, J. Guo, Y. Huang, X. Sun, *Angew. Chem. Int. Ed.* **2024**, *63*, e202314181.

Manuscript received: January 5, 2024
Revised manuscript received: March 28, 2024
Accepted manuscript online: April 3, 2024
Version of record online: April 19, 2024
